



A complex Tibetan upper mantle: A fragmented Indian slab and no south-verging subduction of Eurasian lithosphere

Xiaofeng Liang^a, Eric Sandvol^a, Y. John Chen^{b,*}, Thomas Hearn^c, James Ni^c, Simon Klemperer^d, Yang Shen^e, Frederik Tilmann^{f,g}

^a Department of Geological Sciences, University of Missouri, Columbia, MO 65211, USA

^b Institute of Theoretical and Applied Geophysics, School of Earth and Space Sciences, Peking University, Beijing 100871, China

^c Department of Physics, New Mexico State University, Las Cruces, NM 88003, USA

^d Department of Geophysics, Stanford University, Stanford, CA 94305, USA

^e Graduate School of Oceanography, University of Rhode Island, Narragansett, RI 02882, USA

^f Helmholtz Centre Potsdam – GFZ German Research Centre for Geosciences, Telegrafenberg, 14473 Potsdam, Germany

^g Freie Universität Berlin, Institute for Geological Sciences, Malteserstr. 74-100, 12249 Berlin, Germany

ARTICLE INFO

Article history:

Received 15 November 2011

Received in revised form

27 March 2012

Accepted 30 March 2012

Editor: P. Shearer

Keywords:

Tibetan plateau

Indian lithosphere

fragmentation

Asian continental subduction

finite frequency tomography

ABSTRACT

Due to the non-uniform seismic station coverage in Tibet, critically important questions remain about the existence of southward continental subduction of Eurasia beneath northern Tibet from north, and the nature of the underthrusting Indian lithosphere underneath southern Tibet from south. Using differential P- and S-wave travel-times measured from 301 stations of all the temporary experiments deployed throughout Tibet, we constructed a comprehensive tomographic model. The upper mantle of northern Tibet consists of a rather homogeneous low velocity zone with no evidence of southward Asian continental subduction. In contrast the upper mantle from the Himalayas to central Tibet exhibits laterally variable P- and S-wave velocities. Significant low velocity zones are observed that are elongated in a north–south direction and extending to at least 150 km depth, which we interpret as evidences for fragmentation of the underthrusting Indian continental lithosphere.

© 2012 Elsevier B.V. All rights reserved.

1. Introduction

Over the last two decades, there have been many geological and geophysical studies in the Tibetan plateau including a large number of temporary seismic experiments operated from the Himalayas to the Qaidam Basin and Qilian Shan (Fig. 1). Although receiver function analysis has suggested possible southward subduction of the Asian continental lithosphere beneath northern Tibet (Kind et al., 2002), this interpretation largely relies on visual correlation of scattered arrivals of unknown origin across multiple receivers. Other receiver-function profiles across Tibet fail to show the same structure (Yue et al., submitted for publication; Zhao et al., 2010). Traditional models for the uplift of Tibet typically involve a uniform northward underthrusting Indian continental lithosphere (UICL) in southern Tibet (Barazangi and Ni, 1982; Jin et al., 1996; McNamara et al., 1995). Seismic images from data collected by temporary experiments have concluded that in general the upper-mantle structure beneath the southern Tibetan

plateau, approximately south of the Bangong–Nujiang suture (BNS, Fig. 1), is dominated by the fast P-wave velocity of northward underthrusting of Indian continental lithosphere; however, due in part to the very non-uniform seismic station coverage (Fig. 1), the nature and geometry of the UICL remain poorly understood.

Evidence for the UICL include observations of high Pn velocity and low Sn attenuation (Barazangi and Ni, 1982; McNamara et al., 1995), gravity anomalies (Jin et al., 1996), converted seismic phases in the lower crust and upper mantle (Kind et al., 2002; Nabelek et al., 2009; Owens and Zandt, 1997), shear wave splitting (Fu et al., 2008; Huang et al., 2000) and body-wave tomography (Li et al., 2008; Tilmann et al., 2003). P-wave receiver function profiles perpendicular to the Himalayas reveal double P-to-S converted phases in the southern Tibetan lower crust and Moho, which have been interpreted as evidence for an underthrusting Indian lower crust extending beyond the Indus–Yarlung suture (IYS) to near the BNS (Kind et al., 2002; Nabelek et al., 2009; Schulte-Pelkum et al., 2005) (Fig. 1). Two S-to-P converted-phase images (Kumar et al., 2006; Zhao et al., 2010) and body-wave tomographic models (Li et al., 2008) suggest significant east–west lateral variations in the geometry and thickness of the UICL. From the eastern Himalayan syntaxis to the western edge of

* Corresponding author. Tel.: +86 10 6275 8277; fax: +86 10 6275 8260.
E-mail address: johnyc@pku.edu.cn (Y.J. Chen).

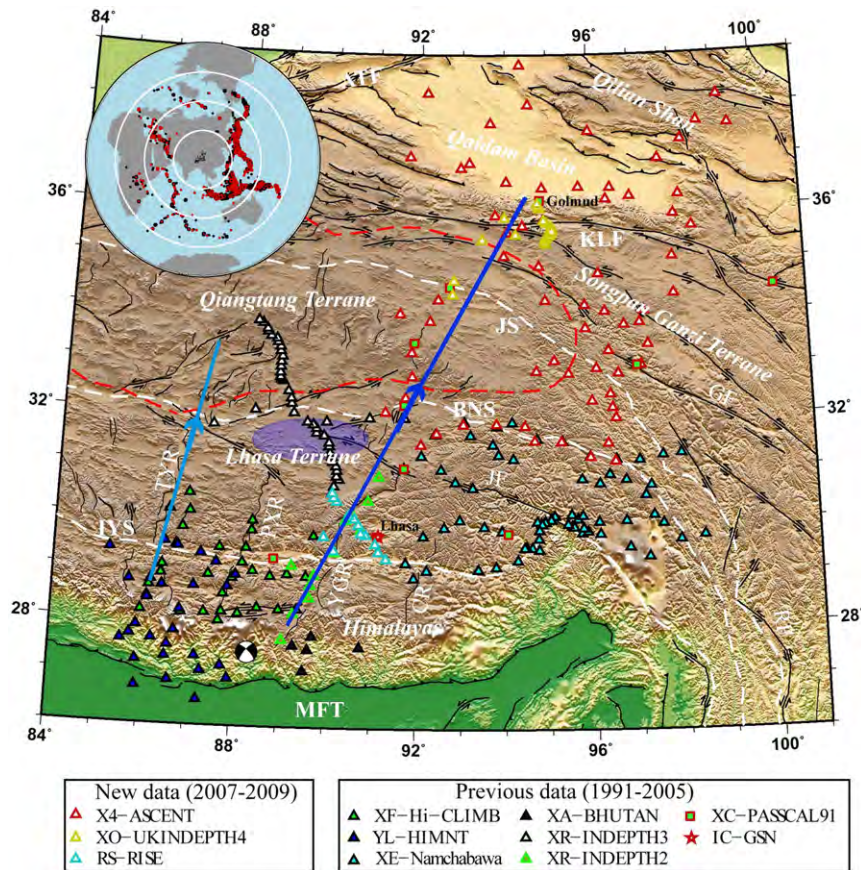


Fig. 1. Tectonic and topographic map of southern and eastern Tibetan Plateau with seismic stations used in this study. The different colors and symbols show the station locations from different experiments. The red dashed line shows the location of the Pn low velocity and Sn high attenuation zone (Barazangi and Ni, 1982; McNamara et al., 1995). The dark blue line (Kind et al., 2002; Zhao et al., 2010) and light blue line (Zhao et al., 2010) show the approximate receiver function profiles location, and the arrows on the lines indicate the subducted Indian continental lithosphere front (Zhao et al., 2010). The dark blue line is almost along the Golmud–Lhasa highway. The blue shaded region shows the high P-wave velocity anomaly imaged from body wave tomography (Tilmann et al., 2003). The map also shows the major thrust faults (MFT: Main Frontal Thrust), sutures (YS: Indus–Yarlung suture, BNS: Bangong–Nujiang suture, JS: Jinsha suture), strike-slip faults (KLF: Kunlun fault, ATF: Altyn Tagh fault, JF: Jiali fault, GF: Ganzi fault, RF: Red River fault), and the north–south trending rifts of southern Tibet (CR: Comei rift, YGR: Yadong–Gulu rift, PXR: Pumqu–Xianza rift, TYR: Tangra Yum Co rift). Geological structures are from the HimaTibetMap-1.0 dataset (Styron et al., 2010). The September 18, 2011 Mw 6.8 Sikkim earthquake is shown as a strike-slip focal mechanism based on the Global CMT catalog. The inset shows earthquakes used in the inversion at epicentral distances of 30–90°. Black circles represent the events with measured P- and PcP-wave travel times, and red circles are those additionally providing S- and ScS-wave data. (For interpretation of the references to color in this figure legend, the reader is referred to the web version of this article.)

the Tarim Basin, the Indian lithosphere appears to be underthrusting Tibet at an increasingly shallower angle and reaching progressively further to the north (Li et al., 2008). Furthermore, two body-wave tomography results (Liang et al., 2011; Ren and Shen, 2008) show some low velocity anomalies beneath southern Tibet, which suggest significant lateral variations within the UICL.

2. Data

Geophysical experiments in Tibet mainly consist of one dimensional linear arrays, but few two dimensional arrays existed before the large-scale INDEPTH IV/ASCENT experiment. The linear arrays do not provide a complete picture of the three dimensional structure of the crust and mantle beneath the plateau. In this study we combine data from ten temporary seismic networks that have been deployed over the past twenty years in the Tibetan plateau including projects INDEPTH IV/ASCENT (Sandvol et al., 2008), RISE (Jin et al., 2009), PASSCAL91 (Owens et al., 1993), Namcha Barwa (Sol et al., 2007), Hi-CLIMB (Nabelek et al., 2009), INDEPTH II (Brown et al., 1996), III (Huang et al., 2000) and IV(UK) (Zhao et al., 2008), BHUTAN (Velasco et al., 2007), and HIMNT (de la Torre and Sheehan, 2005). The combined data set includes 301

stations: 31 from Hi-CLIMB, 28 from HIMNT, 1 from the Global Seismic Network (GSN), 5 from BHUTAN, 12 from INDEPTH II, 42 from INDEPTH III, 19 from INDEPTH IV(UK), 69 from Namcha Barwa, 13 from RISE, 10 from PASSCAL91, and 71 from ASCENT (Fig. 1). Because different frequencies sample different regions along the ray paths (Dahlen et al., 2000). Different frequency band waveform data were extracted in order to apply a finite-frequency travel-time tomography algorithm to image the 3-D P- and S-wave velocity structure beneath southern and eastern Tibet. We selected events with epicentral distances of 30–90° to minimize the interference of long-period waves from the mantle transition zone and core-mantle boundary (Fig. 1) and the events recorded by at least four stations. For example, for the experiments with fewer stations (PASSCAL91, INDEPTH II and BHUTAN), on average events were recorded by 4–9 stations for PASSCAL91, by 8 stations for INDEPTH II, and by 4–5 stations for BHUTAN, whereas for the contemporaneous and overlapping ASCENT and INDEPTH IV(UK) experiments, events were on average recorded at more than 60 stations. Then we hand-picked the arrival times of the P, PcP, S and ScS phases at high- and low-frequency bands (0.5–2 Hz and 0.1–0.5 Hz for P wave, and 0.1–0.5 Hz and 0.05–0.1 Hz for S wave), and obtained the differential travel-times using Multi-Channel Cross-Correlation (MCCC) (VanDecar

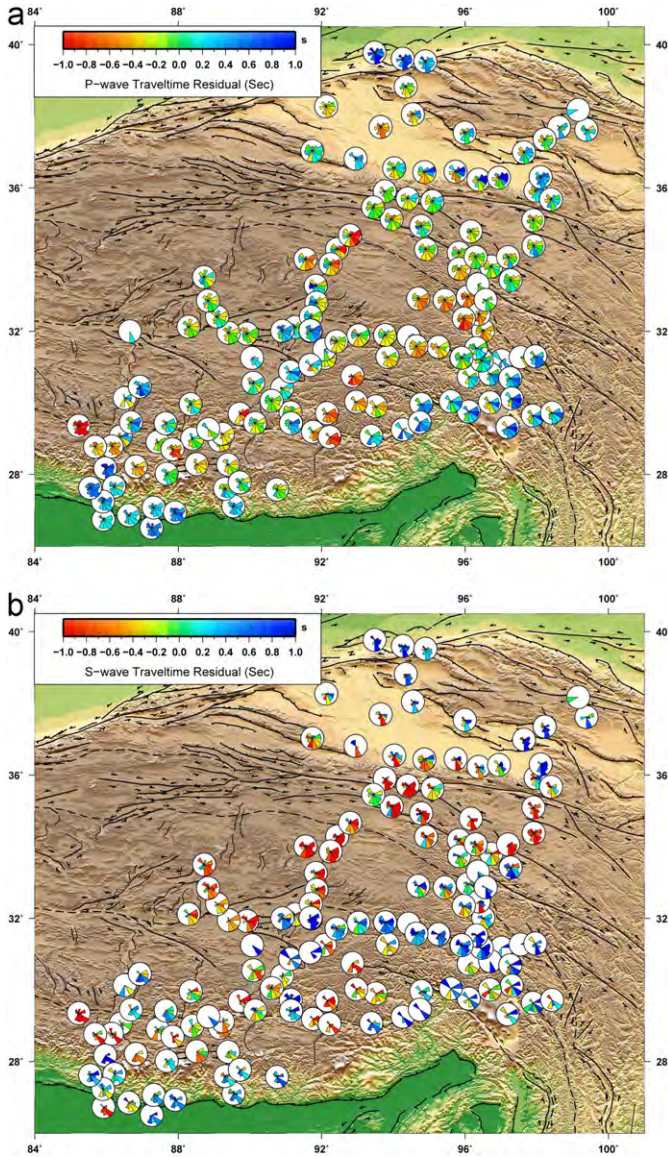


Fig. 2. Sector diagrams of differential travel times, which is averaged in 30° azimuth space at each station. (a) P-wave sector averaged differential travel times. (b) S-wave averaged differential travel times. The sector length shows the normalized measurements number in the 30° azimuth range. The averaged travel time residuals show the travel time differences among different ray paths, which sample the region from the sources to the receivers. Here the different azimuth reflects the different regions sampled by the ray-paths. The amplitude of measurements is shown by the different colors. Selected stations are shown here to avoid overlapping among stations. See [Supplementary Fig. S1](#) for a comprehensive map of all stations. (For interpretation of the references to color in this figure legend, the reader is referred to the web version of this article.)

and Crosson, 1990). The travel times used in the inversion are 86,734 high-frequency and 27,316 low-frequency P waves, and 14,888 high-frequency and 10,692 low-frequency S waves, respectively. Altogether, 114,050 P and PcP picked phases and 25,580 S and ScS picked phases were used. The lateral P- and S-wave velocity variations are directly indicated by travel-times (Fig. 2).

3. Method

In this study, a finite-frequency seismic tomographic method was used to invert for the P- and S-wave crustal and upper mantle velocity structures beneath eastern Tibet although we also tested

more traditional ray-based approaches. The methodology is briefly described here.

3.1. Finite frequency theory

The seismic travel time from the Born–Fréchet travel time sensitivity kernels, which express the influence of velocity perturbations upon a travel time shift when finite frequency effect is included, is written as (Dahlen et al., 2000)

$$\delta t = \iiint_{\oplus} K(x)(\delta c(x)/c(x)d^3x), \quad (1)$$

where K is the 3-D Fréchet sensitivity kernel for a travel time shift δt , measured by cross-correlation of an observed pulse with its spherical Earth assumption. It is expressed by the formulation (Dahlen et al., 2000):

$$K = \frac{1}{2\pi c} \left(\frac{R}{c_r R' R''} \right) \times \frac{\int_0^\infty \omega^3 |s_{syn}(\omega)|^2 \sin(\omega \Delta T) d\omega}{\int_0^\infty \omega^2 |s_{syn}(\omega)|^2 d\omega}, \quad (2)$$

where ΔT represents the difference in travel time between the path with a detour through a single point scatterer between the source and receiver relative to the corresponding direct path; R , R' and R'' are geometrical spreading factors for the unperturbed ray, the forward source-to-scatterer ray and the backward receiver-to-scatterer ray, respectively. The presence of the power spectrum of the synthetic pulse $|s_{syn}|^2$ shows effectively the frequency dependency of the cross-correlated differential travel times.

Here, for our regional travel-time tomography the relative arrival times of P or S phases at a number of stations are measured by MCCC to constrain spatial variations of underlying mantle velocity perturbations. The finite volume sensitivity of a relative delay between two nearby stations 1 and 2, $\delta t_1 - \delta t_2$, is simply the difference of the individual Fréchet kernels for the travel time shifts, δt_1 and δt_2 , when we take one station as reference (Hung et al., 2004)

$$K_{\delta t_1 - \delta t_2} = K_{\delta t_1} - K_{\delta t_2}. \quad (3)$$

Because there is the same structure between the equations for the banana-doughnut travel time residual and ray-path travel time residual, our measured data d_i of P and S differential travel times can be inverted to produce tomographic models of velocity perturbations using the same linear equation by using Born–Fréchet travel time sensitivity kernels instead of ray-path segments to construct the coefficient matrix (Chiao and Kuo, 2001; Hung et al., 2004):

$$d_i = \int_D g_i(x)m(x)d^3x, \quad (4)$$

where d_i , $i=1 \dots N$, represents the i th differential travel time data; x is the position vector in 3-D model space, D ; and g_i represents the 3-D Fréchet sensitivity kernel corresponding to the data d_i with the model function $m(x)$. We have tested the effects of applying the finite-frequency approach by also using a classical ray-tracing approach. We found that our finite-frequency and ray theory images were essentially equivalent for the large features interpreted in this study (see [Supplementary material Fig. S10](#) in the Appendix). Because teleseismic differential travel-times are being measured, only lateral velocity contrasts can be resolved.

3.2. Model parameterization and inversion

The crustal and mantle volume beneath the study area was parameterized with a regular $65 \times 65 \times 33$ grids centered at (94.5°E , 33°N), and had a dimension of 30° in longitude, 30° in latitude, and 1200 km in depth. The model was made big enough to completely include the differential travel time sensitivity

kernels in our model space. It resulted in a cell spacing of $\sim 0.47^\circ$ in longitude and latitude and 37 km in depth. Every cell has uniform velocity during the inversion. With this parameterization, the travel time equations can be written as:

$$d_i = G_{il}m_l, \quad (5)$$

where d_i is the i th differential travel time data, and G_{il} is the differential value of the integrated volumetric kernels of the i th event contributing to the l th node and m_l , the model parameter at the l th node. The inversion problem was resolved by the standard damped least-squares method (Paige and Saunders, 1982):

$$\hat{m} = (G^T G + \theta^2 I)^{-1} G^T d, \quad (6)$$

where I is the identity matrix. The damping parameter θ is determined empirically through examining the variance reduction versus the model norm represented by a trade-off curve. We chose the damping parameter that yields an optimum variance reduction and a relatively small model norm (see Supplementary Fig. S5 in the Appendix). The model discussed in this paper is obtained using a damping parameter that yields a variance reduction of $\sim 55\%$ for P-wave and $\sim 53\%$ for S-wave. The lower variance reduction of the P-velocity model reflects influence from the data redundancy for the mixed-determined linear system. Here we apply an equal-weight scheme for the events within a 5° azimuth and 10° epicentral distance sector, recorded by the same station. A weight was assigned to the travel times based on how many events from the same azimuth and epicentral distance range were recorded by the stations, and the weight was equal to the reciprocal value of the number of events in that azimuth and epicentral distance bin. This weight scheme was applied to partly compensate for uneven event distribution, which can otherwise produce prominent streaks along the directions taken by more rays (Humphreys and Clayton, 1988), or travel-time sensitivity kernels here. The weighted inversions also improve the variance reduction by decreasing the weight of data with larger variance (see Supplementary Fig. S5 in the Appendix).

3.3. Crustal and elevation correction

The travel time anomalies can be caused by crustal thickness variations, station elevations and lateral velocity heterogeneities. Since the ray paths of teleseismic body waves are nearly vertical near the surface, the depth of ray-path crossing is usually deep and shallow velocity structures are thus poorly constrained by relative travel time data in the inversion. Therefore, the crustal correction is also an important component in order to reduce the tradeoff between crustal and mantle velocity heterogeneities in teleseismic travel-time tomography. To correct for the crustal effects, the frequency-dependent crustal correction for each event-station record was calculated from the synthetic crustal response of an incoming plane wave beneath the station (Yang and Shen, 2006). We have tested several different crustal models: CUB2.0 (Ritzwoller et al., 2002), CRUST2.0 (Bassin et al., 2000) and SEAPS (Sun et al., 2004, 2008). In general we did not find any large differences in the large-scale features (> 200 -km), except when using extreme, probably unreasonable crustal thickness values, such as very abrupt (15 km or larger) changes in Moho depth. We used the crustal structure from SEAPS (Sun et al., 2004, 2008) for most of stations, except using CRUST2.0 (Bassin et al., 2000) for several stations in the Sub-Himalaya where SEAPS is not defined (see Supplementary material Figs. S2 and S3 in the Appendix). The differential travel times after crustal correction show no significant influence from crustal structure (see Supplementary material Fig. S4 in the Appendix). An additional free term for each station was incorporated into the inversion to absorb travel-time shifts

caused by remaining shallow heterogeneity (see Supplementary material Fig. S13 in the Appendix).

3.4. Resolution tests

Three-dimensional resolution tests were performed to evaluate the data coverage and the ability of the inversion to recover the mantle structure (see Supplementary Figs. S6, S7, S8, S9, S10 and S11 in the Appendix). For this purpose, the synthetic travel times were computed by multiplying the G -matrix with different input velocity models: $\Delta t_{syn} = G \cdot \Delta c_{syn} + t_{noise}$, where t_{noise} is random noise added to the synthetic travel times, which follows a Gaussian distribution with standard deviation of 0.1 s, which about 10% of the typical differential travel time span for an event. The inversion was then performed using the same damping parameter as that used in the inversion of real data. The checkerboard resolution tests were conducted using input anomalies with a diameter of 150 km. The magnitude of the velocity perturbation decreases from the center of the checkerboard cells to zero at the boundaries as a cosine function. The maximum velocity perturbation is $\pm 2\%$ for P wave and $\pm 4\%$ for S wave. The checkerboard resolution tests strongly suggest that the input anomalies are recovered reasonably well in the region with good ray path coverage. At the same time the anomaly intensity is strongly damped during the inversion to about 1/3 to 1/2 of the input anomaly intensity.

4. Results and discussions

By combining all the available data in this study, we are able to obtain the most comprehensive 3-D picture of the crustal and upper mantle beneath the Himalaya and Tibet encompassing the largest number of stations in Eastern Tibet to date (Figs. 3 and 4). These images provide new insights into the important unresolved questions concerning the tectonic evolution of the Tibetan plateau: whether there is south-verging continental subduction along the southern margin of the Qaidam basin (Tapponnier et al., 2001) and the geometry and location of the UICL.

4.1. South verging Asian lithospheric subduction

We observe a sharp velocity contrast boundary in the upper 200-km between the Qaidam basin and the Kunlun mountain in northern Tibet (Figs. 3 and 4). This boundary is close to the Kunlun fault (KLF) between 93° and 98° E, and essentially vertical. The upper mantle of the northern Qiangtang terrane and Songpan-Ganzi terrane shows a homogeneously slow uppermost mantle (relative to southern Tibet) (Figs. 4 and 5), which extends down to at least 250 km with no evidence of any high velocity body beneath northern Tibet. The LVZ between 91° to 93° E extends south to about 32.5° N (close to BNS) but from 95° to 99° E only to about the Jinsha suture (JS). The P-wave LVZ appears to extend deeper than 300 km. The amplitude of this anomaly is consistent with a temperature anomaly of about $+300^\circ$ C (Wittlinger et al., 1996), however, it is important to note that the magnitude of this anomaly is highly dependent upon the choice of damping parameter in our inversion. P-wave travel-time tomography images along the Golmud–Lhasa highway in northern Tibet by Wittlinger et al. (Wittlinger et al., 1996) shows a bulky low velocity zone (LVZ) starting at about 150 km beneath the northernmost Tibetan plateau. The cross-sections along the similar position from our result show the similar result, although entirely independent data sets are used (Fig. 5, right).

The LVZ has a slower velocity with respect to the high velocity upper mantle beneath the Qaidam basin, so this anomaly cannot

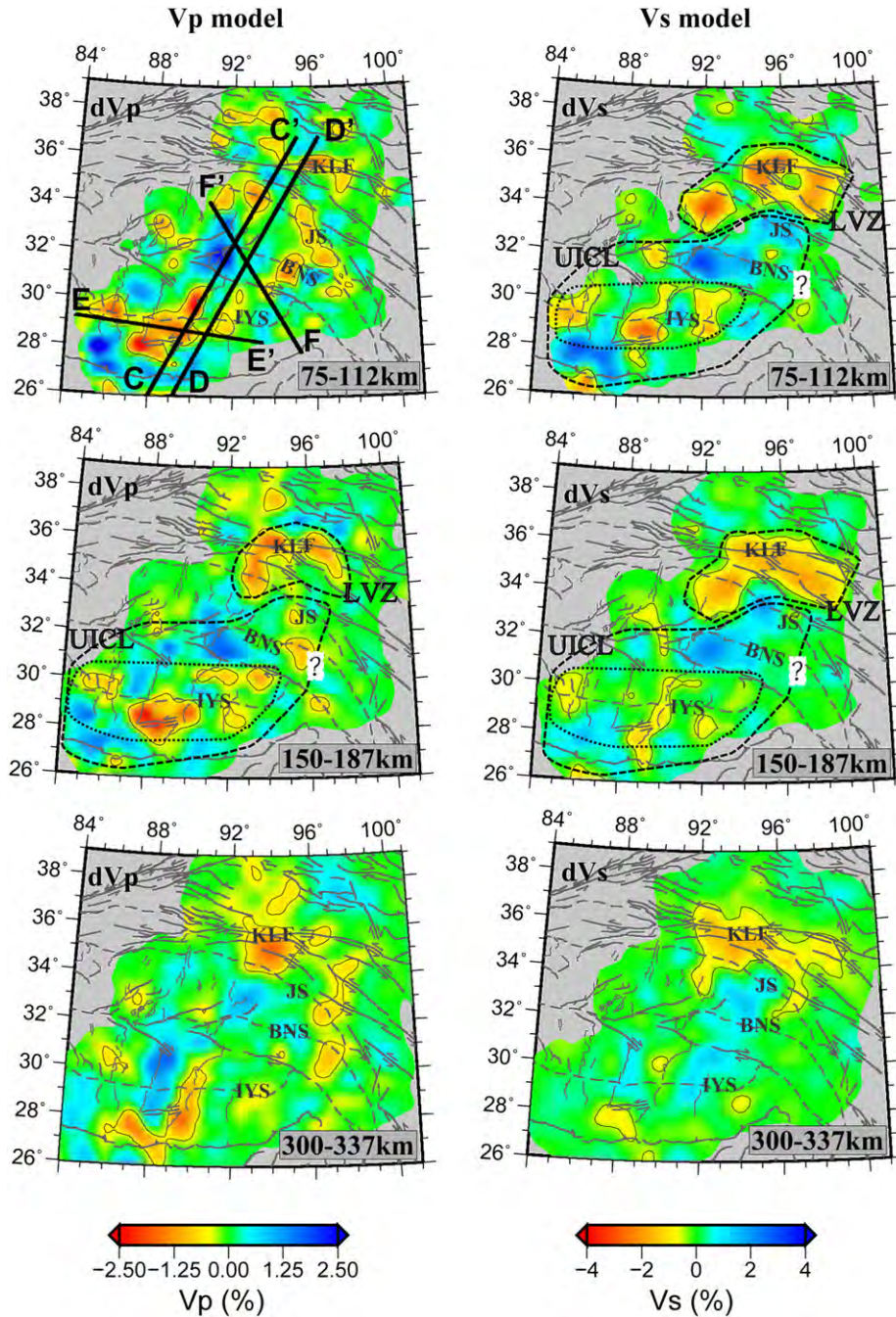


Fig. 3. Velocity structures beneath southern and eastern Tibet obtained from our finite-frequency teleseismic travel-time tomography. Horizontal slices of the P- and S-wave velocities are shown at depths of 75–112 km, 150–187 km, and 300–337 km. The Vp and Vs images are clipped based on the data coverage (the kernel intensity for P and S travel-time sensitivity kernels). The UICL and upper-mantle LVZ of northern Tibet are encircled by black dashed lines. The alternating low and high velocity anomalies of southern Tibet, interpreted as the UICL fragments, are encircled by black dotted lines. The geological structures of Fig. 1 are shown as gray lines.

be a lateral continuation of the Asian lithosphere, unless the lithosphere subducting from the north has been heated up considerably. Within the resolution of our tomography, this observation suggests that there is little subduction or underthrusting of the Qaidam basin lithosphere beneath northeastern Tibet. The resolution test with two input synthetic high velocities beneath Songpan-Ganzi terrane and southern Tibet shows that there is reasonably good resolution for our tomographic model for the presumed subducted Eurasian and Indian lithosphere (Fig. 6). Recent images using surface-wave tomography (Ceylan et al., 2010) show a similar result. The southward dipping conversion beneath the KLF and northern Tibet along 93°E longitude, interpreted as subducted Asian mantle lithosphere (Kind et al., 2002),

may instead be either P-to-S multiples or fossil lithospheric mantle boundary (Yue et al., submitted for publication). It is important to note that P-to-S receiver functions are usually noisy and ambiguous in this depth range, and that these converters are not consistently observed between different data sets (i.e. the P-wave and S-wave receiver functions show very different images (Kind et al., 2002; Kumar et al., 2006; Zhao et al., 2010)).

The previous geology and geophysics work in this area (Wang et al., 2011; Yin et al., 2008; Yin et al., 2007) using surface mapping and dense seismic reflection profiles across Qaidam basin found that all the observed thrusts are north-dipping rather than south-dipping thrusts in the upper crust. In order to reconcile the seismic imaging of Kind et al. (2002), geologists

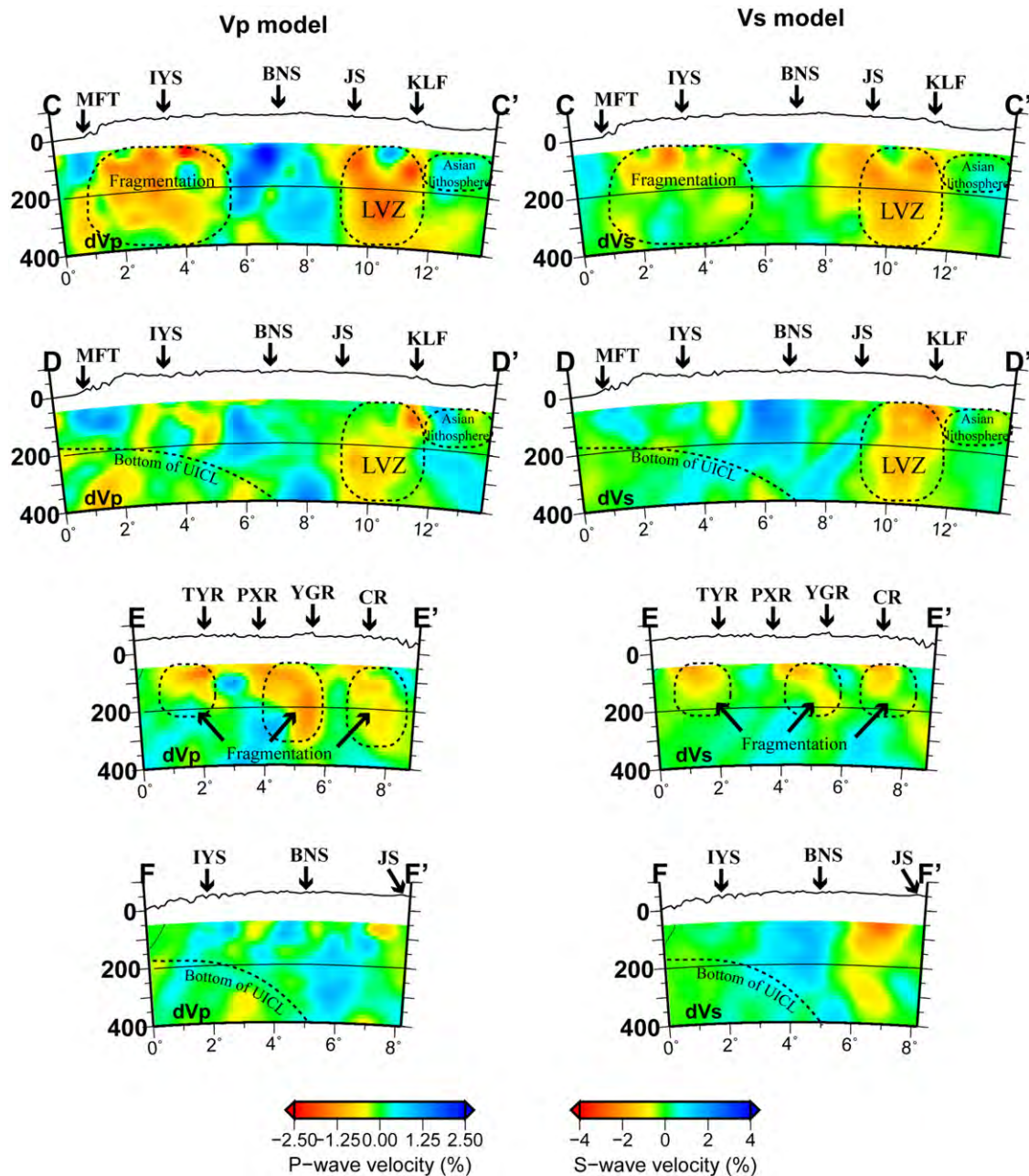


Fig. 4. N–S vertical cross-sections for P-wave and S-wave velocity structures are shown along the CC', DD', EE' and FF' profiles in Fig. 3. Topography on the vertical sections is exaggerated 10 times. The dashed lines show the interpreted features along the different cross-sections. Because of the limited recovery for the crustal structure, we only show the velocities below 50 km depth.

tried to use 'flake' tectonics to reconcile the differences (Wang et al., 2011; Yin et al., 2008). In light of recent receive-function imaging of the Moho geometry across the eastern Kunlun, the Moho below the Kunlun is offset by north-dipping lithospheric-scale thrusts (Shi et al., 2009). The deep seismic reflection results also suggest that the Songpan-Ganzi lower crust was underthrusting or flowing beneath the Qaidam basin (Karplus et al., 2011; Wang et al., 2011). These studies are more consistent with our tomographic results in that there is no significant southward subduction of Asian lithosphere in the upper mantle. The integration of the existing studies mentioned above and our results seem to provide a coherent and persuasive argument against the existence of southward subduction of the Asian lithosphere.

There are several possible alternative origins of this LVZ. Mid-Miocene to Quaternary volcanics scattered across the Songpan-Ganzi

terranes that die out east of 92°E include volumetrically minor leucogranites (crustal melts) but are dominantly shoshonitic melts from lithospheric mantle sources (Chung et al., 2005). Both the LVZ and shoshonitic volcanics could be related to viscous strain heating in the uppermost mantle (Nabelek et al., 2010), and a back-arc convective flow induced by the subducted continental Indian mantle lithosphere (Tilmann et al., 2003) or mantle upwelling related to lithospheric delamination (Molnar et al., 1993). Given the observations of a 130–150 km thick lithosphere in northern Tibet (Kumar et al., 2006; Yue et al., submitted for publication; Zhao et al., 2011), it seems unlikely we are seeing the evidence of either convective removal or a lithospheric delamination. The LVZ is centered on a region with the largest shear-wave splitting delay times in the entire plateau. Shear-wave splitting studies have shown a very strong east-west anisotropic fabric (Huang et al., 2000; Leon Soto et al., 2010;

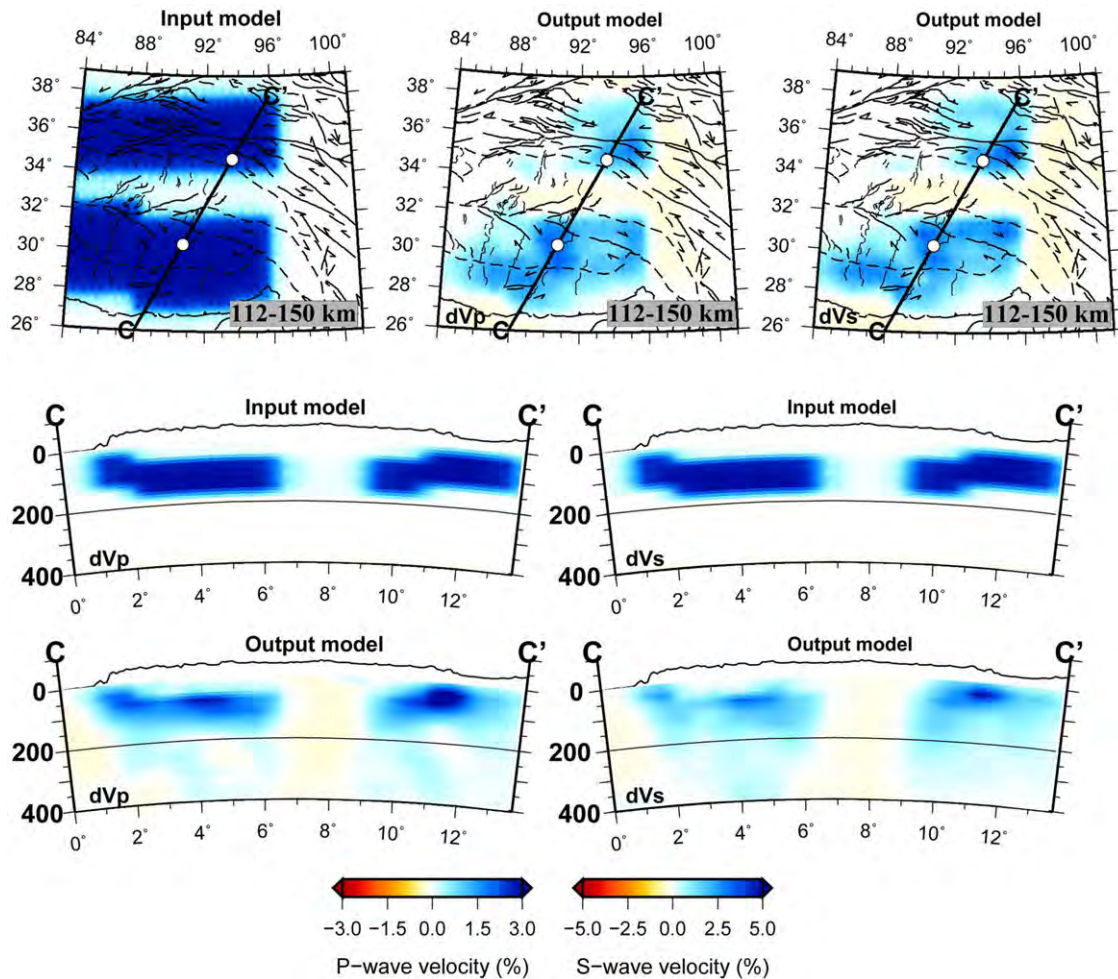


Fig. 6. A resolution test for both P- and S-wave models with two input high velocity slabs. The two input slabs are corresponding to subducted Indian lithosphere from south and subducted Asian lithosphere from north. The inverted models show that the slabs are recovered continuously.

tomographic cross-section from Li et al. (2008) is quite similar to our image along the N–S profile of 90°E, where similar data are used in the two studies. It is likely that the difference in mantle velocity structure of central-northeastern Tibet between our results and Li et al. (2008) is attributed to our addition of many new data from the ASCENT seismic experiment. The UICL penetrates about 100 km further north than suggested from prior seismic observations in eastern central Tibet (along the Golmud–Lhasa highway) (Chen and Ozalaybey, 1998; Kumar et al., 2006; Li et al., 2008; Tilmann et al., 2003; Zhao et al., 2010), consistent with recent surface-wave tomographic results (Ceylan et al., 2010). The P-wave tomographic image of the upper mantle beneath central Tibet from INDEPTH III data has revealed a sub-vertical high velocity zone from about 100 km to 400 km depth, located approximately south of the BNS, which is interpreted as the downwelling Indian mantle lithosphere (Tilmann et al., 2003): our 3-D images show a high velocity body at a similar location (Fig. 5, left).

Our results show significant low-velocity anomalies in the upper mantle beneath southern Tibet (Figs. 3 and 4), which confirm the geometry and depth extent of the low P- and S-wave velocities found by recent regional finite-frequency tomography studies (Liang et al., 2011; Ren and Shen, 2008). The UICL is clearly not uniform and has significant orogen-parallel variations in both P- and S-wave upper-mantle velocities, because the resolution test shows our data set is able to image a uniform subducted high velocity subducted Indian lithosphere beneath

southern Tibet (Fig. 6). The UICL is more complex than suggested by interpretations of the linear seismic profiles in southern Tibet. Furthermore, because we have been able to construct an image of the eastern half of the Tibetan plateau, we can now be certain that these velocity differences are not small inhomogeneities within the UICL but instead are likely to be as large as the well-known velocity contrast between northern and southern Tibet. These alternating high- and low-velocities are tested using a large number of synthetic tests, different algorithms and crustal corrections to ensure they are reliable (Fig. 7). These tests show the anomalies are not caused by smearing of crustal low-velocities during the inversions. The shallow low-velocity anomalies (75–112 km depth) are spatially correlated with the Coma, Yadong-Gulu, and Tangra Yum Co rifts from east to west, and they appear to extend to at least 150 km depth. However, the relationship between the shallow rift basins and the deep low velocity anomaly is by no means obvious. Pn tomographic models also show a similar pattern of alternating high and low velocities for the uppermost mantle beneath southern Tibet (Liang and Song, 2006; Wang et al., 2010). It is possible that these low-velocity anomalies beneath southern Tibet are due to compositional variation within the UICL formed perhaps during a Permo-Triassic rifting event along the northern Indian passive margin. Alternatively, these inter-UICL heterogeneities might be Archean cratonic nuclei and/or Proterozoic mobile belts formed during the assembly of the India plate. However, given the strength of these velocity anomalies and likelihood that the UICL has undergone

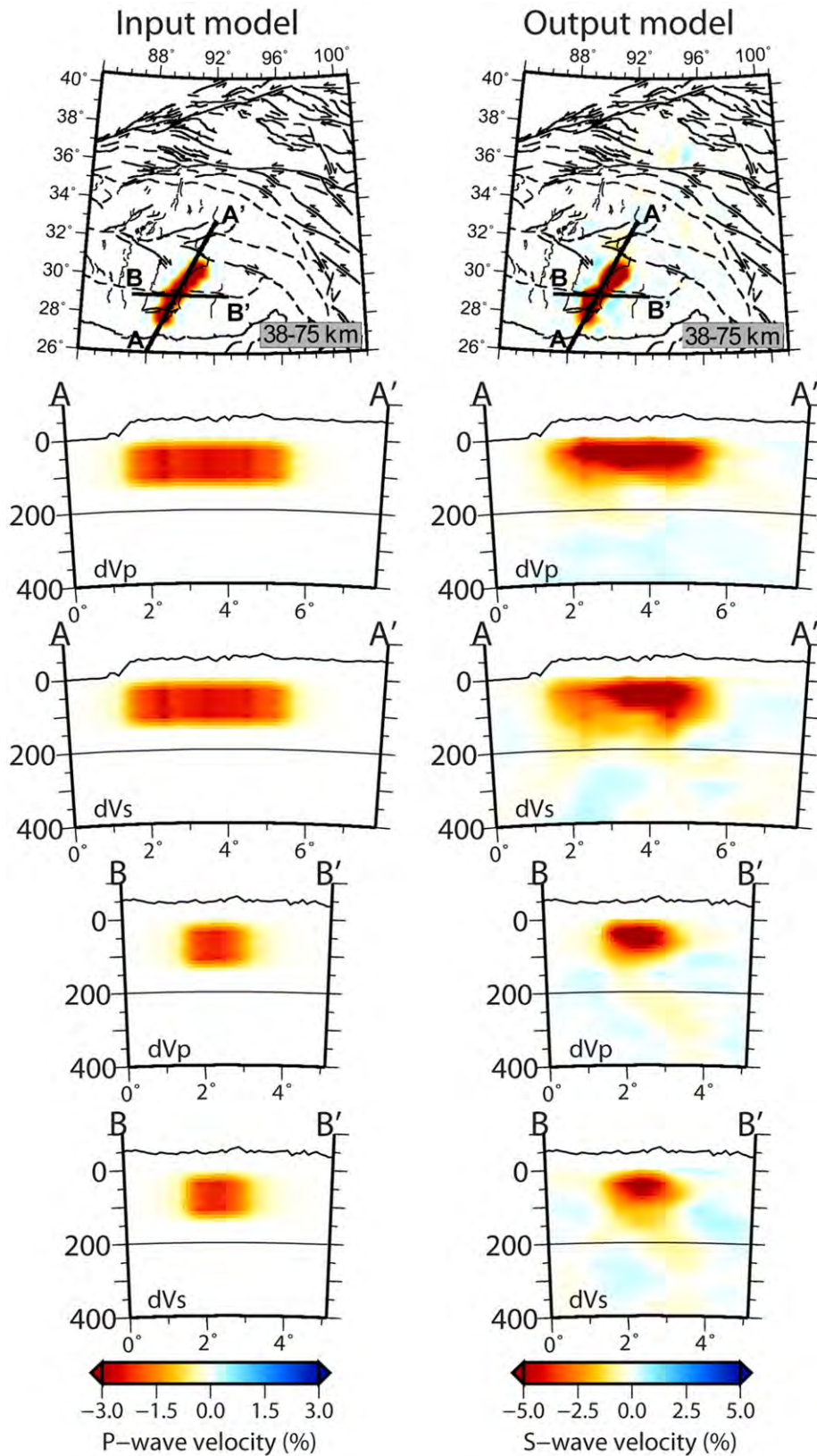


Fig. 7. The results of one of our resolution tests for both compressional- and shear-wave models along YGR show the robustness of the low-velocity anomalies. There is little depth smearing for shallow structures located in the upper 110 km.

substantial deformation during underthrusting, we consider that these low velocities are most likely the consequence of recent fragmentation of the Indian lithosphere (Liang et al., 2011) (Fig. 8). It is less likely that this fragmentation is associated with

the surface rifting (Ren and Shen, 2008; Yin, 2000), since many of the sub-Moho earthquakes (~80–95 km) in southernmost Tibet have a large strike-slip rather than normal component (de la Torre et al., 2007). The September 18th, 2011 Mw 6.8 Sikkim event

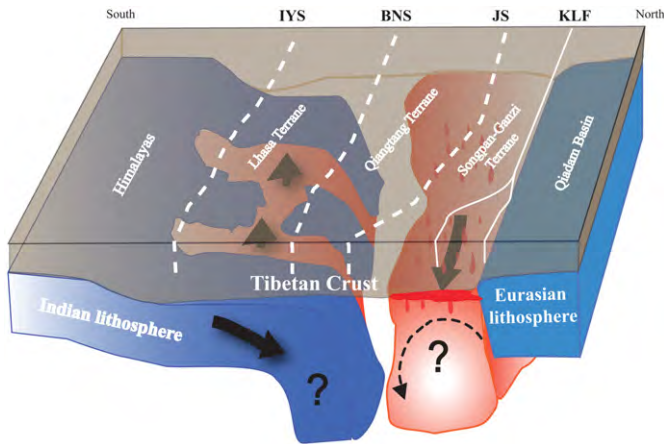


Fig. 8. A cartoon illustrating our interpretation of the current structure of the upper mantle beneath the Tibetan plateau. The fragmented UICL is helping to push or squeeze the asthenosphere beneath northern Tibet with an uneven front. The lithospheric mantle of the northern Tibet is heated by both viscous strain heating and small scale mantle convection induced by the downwelling of UICL. The black arrows show the movement direction of mantle materials.

located south of YGR also shows a strike-slip focal mechanism with 47 km focal depth based on the result from the Global CMT catalog (Fig. 1). The inference that Tibet's shallow rifts extend through the whole lithosphere was proposed as a mechanism for the initiation of the rifts in southern Tibet (Yin, 2000). This model, however, relied on an unrealistic uniform E–W extension model with unreasonable continuous stress boundaries in a multi-layered mechanical rifting model. However it cannot be ruled out that the surface rifts are the potential consequence of the local upwelling of asthenosphere from the fragmentation. We suggest that the present fragmentation is resulting from the curvature of the Himalayan subduction front (McCaffrey and Nabelek, 1998; Seeber and Armbruster, 1984) and the rolling back of the Burma arc (Rao and Kalpna, 2005).

5. Conclusions

From our tomographic work we have imaged a rather homogeneous low-velocity upper mantle beneath the northern Qiangtang and Songpan–Ganzi terranes in northern Tibet, indicative of a warmer uppermost mantle that is inconsistent with the presence of subducted Eurasian continental lithosphere beneath northern Tibet. Higher temperatures and thus lower seismic velocities beneath northern Tibet could have been caused by viscous shear-strain heating of the lithospheric mantle that is being shortened between the Indian and Eurasian cratons. We have also imaged a seismically faster, presumably colder continental lithospheric mantle beneath southern and central Tibet; we interpret this as the UICL which extends northward to the BNS in central Tibet and to JS in eastern Tibet. In southern Tibet, we observe alternating low and high velocity anomalies that have a dominant NNE trend, approximately parallel to the direction of plate convergence. The low velocity anomalies extend to at least 150 km depth. These anomalies indicate significant lateral physical or compositional difference within the UICL, likely due to fragmentation during the underthrusting of the Indian continental lithosphere (Fig. 8).

Acknowledgments

We thank the Seismotectonics group at Peking University and the INDEPTH IV/ASCENT team, who collected a large part of the

data used in this study, as well as the seismic equipment pools PASSCAL and SeisUK (GEF of NERC, loan 767) for support and instrumentation. We also acknowledge the IRIS DMC and the INDEPTH II&III, HIMNT, Namcha Barwa, PASSCAL91, Hi-CLIMB and BHUTAN experiments for collecting seismic data. Steve Roecker kindly shared his ray-theory tomography code with us for comparison of results. Mian Liu gave valuable comments to improve the manuscript. Seismic Analysis Code (SAC) was used for data processing. The Generic Mapping Tools (GMT) was used to produce the figures. This work is supported by the NSF of China under Grant nos. 40520120222 and 0821062; and Continental Dynamics, National Science Foundation under Grant nos. EAR-0634903, EAR-0409589, EAR-0409870, and EAR-0738779.

Appendix A. Supplementary material

Supplementary data associated with this article can be found in the online version at [doi:10.1016/j.epsl.2012.03.036](https://doi.org/10.1016/j.epsl.2012.03.036).

References

- Barazangi, M., Ni, J., 1982. Velocities and propagation characteristics of Pn and Sn beneath the Himalayan arc and Tibetan Plateau: possible evidence for underthrusting of Indian continental lithosphere beneath Tibet. *Geology* 10, 179–185.
- Bassin, C., Laske, G., Masters, G., 2000. The current limits of resolution for surface wave tomography in North America. *EOS Trans. AGU* 81, 897.
- Brown, L.D., Zhao, W.J., Nelson, D.K., Hauck, M., Alsdorf, D., Ross, A., Cogan, M., Clark, M., Liu, X.W., Che, J.K., 1996. Bright spots, structure, and magmatism in southern Tibet from INDEPTH seismic reflection profiling. *Science* 274, 1688–1690.
- Ceylan, S., Ni, J.F., Chen, Y.J., Tilmann, F., Yang, Y., Ritzwoller, M.H., Sandvol, E.A., 2010. 3D Shear Wave Velocity Structure and Seismic Anisotropy beneath Northern Tibet. *AGU 2010 Fall Meeting (abstract T34A-04)*.
- Chen, W.P., Ozalaybey, S., 1998. Correlation between seismic anisotropy and Bouguer gravity anomalies in Tibet and its implications for lithospheric structures. *Geophys. J. Int.* 135, 93–101.
- Chiao, L.Y., Kuo, B.Y., 2001. Multiscale seismic tomography. *Geophys. J. Int.* 145, 517–527.
- Chung, S.-L., Chu, M.-F., Zhang, Y., Xie, Y., Lo, C.-H., Lee, T.-Y., Lan, C.-Y., Li, X., Zhang, Q., Wang, Y., 2005. Tibetan tectonic evolution inferred from spatial and temporal variations in post-collisional magmatism. *Earth Sci. Rev.* 68, 173–196.
- Dahlen, F.A., Hung, S.-H., Nolet, G., 2000. Frechet kernels for finite-frequency traveltimes—I. Theory. *Geophys. J. Int.* 141, 157–174.
- de la Torre, T., Sheehan, A., 2005. Broadband seismic noise analysis of the Himalayan Nepal Tibet seismic experiment. *Bull. Seismol. Soc. Am.* 95, 1202–1208.
- de la Torre, T.L., Monsalve, G., Sheehan, A.F., Sapkota, S., Wu, F., 2007. Earthquake processes of the Himalayan collision zone in eastern Nepal and the southern Tibetan Plateau. *Geophys. J. Int.* 171, 718–738.
- DeCelles, P.G., Robinson, D.M., Zandt, G., 2002. Implications of shortening in the Himalayan fold-thrust belt for uplift of the Tibetan Plateau. *Tectonics* 21, 1062.
- Flesch, L.M., Holt, W.E., Silver, P.G., Stephenson, M., Wang, C.-Y., Chan, W.W., 2005. Constraining the extent of crust–mantle coupling in central Asia using GPS, geologic, and shear wave splitting data. *Earth Planet. Sci. Lett.* 238, 248–268.
- Fu, Y.V., Chen, Y.J., Li, A., Zhou, S., Liang, X., Ye, G., Jin, G., Jiang, M., Ning, J., 2008. Indian mantle corner flow at southern Tibet revealed by shear wave splitting measurements. *Geophys. Res. Lett.* 35, L02308.
- Huang, W.C., Ni, J.F., Tilmann, F., Nelson, D., Guo, J.R., Zhao, W.J., Mechie, J., Kind, R., Saul, J., Rapine, R., Hearn, T.M., 2000. Seismic polarization anisotropy beneath the central Tibetan Plateau. *J. Geophys. Res.* 105, 27979–27989.
- Humphreys, E., Clayton, R., 1988. Adaptation of back projection tomography to seismic travel time problems. *J. Geophys. Res.* 93, 1073–1085.
- Hung, S.-H., Shen, Y., Chiao, L.-Y., 2004. Imaging seismic velocity structure beneath the Iceland hot spot: a finite frequency approach. *J. Geophys. Res.* 109, B08305.
- Jin, G., Chen, Y., Basang, C., 2009. Investigation of local earthquakes in the Lhasa region. *Chin. J. Geophys.* 52, 3020–3026.
- Jin, Y., McNutt, M.K., Zhu, Y., 1996. Mapping the descent of Indian and Eurasian plates beneath the Tibetan Plateau from gravity anomalies. *J. Geophys. Res.* 101, 11275–11290.
- Karplus, M.S., Zhao, W., Klemperer, S.L., Wu, Z., Mechie, J., Shi, D., Brown, L.D., Chen, C., 2011. Injection of Tibetan crust beneath the south Qaidam Basin: evidence from INDEPTH IV wide-angle seismic data. *J. Geophys. Res.* 116, B07301.
- Kind, R., Yuan, X., Saul, J., Nelson, D., Sobolev, S.V., Mechie, J., Zhao, W., Kosarev, G., Ni, J., Achauer, U., Jiang, M., 2002. Seismic images of crust and upper mantle

- beneath Tibet: evidence for Eurasian plate subduction. *Science* 298, 1219–1221.
- Kumar, P., Yuan, X., Kind, R., Ni, J., 2006. Imaging the colliding Indian and Asian lithospheric plates beneath Tibet. *J. Geophys. Res.* 111, B06308.
- Leon Soto, G., Sandvol, E.A., Flesch, L., Ni, J.F., Hearn, T.M., Tilmann, F.J., Chen, Y.J., Brown, L.D., 2010. Significant Seismic Anisotropy Beneath Northeastern Tibet: Implications for Continuous Deformation Processes of Eastern Tibet. 2010 Fall Meeting, AGU (abstract T31E-07).
- Li, C., Hilst, R.D. v.d., Meltzer, A.S., Engdahl, E.R., 2008. Subduction of the Indian lithosphere beneath the Tibetan Plateau and Burma. *Earth Planet. Sci. Lett.* 274, 157–168.
- Liang, C., Song, X., 2006. A low velocity belt beneath northern and eastern Tibetan Plateau from Pn tomography. *Geophys. Res. Lett.* 33, 1–5.
- Liang, X., Shen, Y., Chen, Y.J., Ren, Y., 2011. Crustal and mantle velocity models of southern Tibet from finite frequency tomography. *J. Geophys. Res.* 116, B02408.
- McCaffrey, R., Nabelek, J., 1998. Role of oblique convergence in the active deformation of the Himalayas and southern Tibet plateau. *Geology* 26, 691–694.
- McNamara, D.E., Owens, T.J., Silver, P.G., Wu, F.T., 1994. Shear wave anisotropy beneath the Tibetan Plateau. *J. Geophys. Res.* 99, 13655–13665.
- McNamara, D.E., Owens, T.J., Walter, W.R., 1995. Observations of regional phase propagation across the Tibetan Plateau. *J. Geophys. Res.* 100, 22215–22229.
- Molnar, P., England, P., Martinod, J., 1993. Mantle dynamics, uplift of the Tibetan Plateau, and the Indian Monsoon. *Rev. Geophys.* 31, 357–396.
- Nabelek, J., Hetenyi, G., Vergne, J., Sapkota, S., Kafle, B., Jiang, M., Su, H.P., Chen, J., Huang, B.S., Team, H.-C., 2009. Underplating in the Himalaya-Tibet collision zone revealed by the Hi-CLIMB experiment. *Science* 325, 1371–1374.
- Nabelek, P.L., Whittington, A.G., Hofmeister, A.M., 2010. Strain heating as a mechanism for partial melting and ultrahigh temperature metamorphism in convergent orogens: implications of temperature-dependent thermal diffusivity and rheology. *J. Geophys. Res.* 115, 1–17.
- Owens, T.J., Randall, G.E., Wu, F.T., Zeng, R., 1993. PASSCAL instrument performance during the Tibetan Plateau passive seismic experiment. *Bull. Seismol. Soc. Am.* 83, 1959–1970.
- Owens, T.J., Zandt, G., 1997. Implications of crustal property variations for models of Tibetan Plateau evolution. *Nature* 387, 37–43.
- Paige, C., Saunders, M.A., 1982. LSQR: an algorithm for sparse linear equations and sparse least squares. *ACM Trans. Math. Softw.* 8, 43–71.
- Rao, N.P., Kalpa, 2005. Deformation of the subducted Indian lithospheric slab in the Burmese arc. *Geophys. Res. Lett.* 32, 1–5.
- Ren, Y., Shen, Y., 2008. Finite frequency tomography in southeastern Tibet: evidence for the causal relationship between mantle lithosphere delamination and the north–south trending rifts. *J. Geophys. Res.* 113, B10316.
- Ritzwoller, M.H., Shapiro, N.M., Barmin, M.P., Levshin, A.L., 2002. Global surface wave diffraction tomography. *J. Geophys. Res.* 107, 2335.
- Sandvol, E., Chen, J., Ni, J., Zhou, S., Ma, Y., Zhang, X., Yue, H., Ceylan, S., Bao, X.C., Hearn, T., 2008. Lithospheric Seismic Velocity Structure of the Northern Tibetan Plateau: The ASCENT Seismic Experiment. EOS, Transactions American Geophysical Union, vol. 89, Fall Meeting Supplement (abstract S14A-01).
- Schulte-Pelkum, V., Monsalve, G., Sheehan, A., Pandey, M.R., Sapkota, S., Bilham, R., Wu, F., 2005. Imaging the Indian subcontinent beneath the Himalaya. *Nature* 435, 1222–1225.
- Seeber, L., Armbruster, J.G., 1984. Some elements of continental subduction along the Himalayan front. *Tectonophysics* 105, 263–278.
- Shi, D., Shen, Y., Zhao, W., Li, A., 2009. Seismic evidence for a Moho offset and south-directed thrust at the easternmost Qaidam–Kunlun boundary in the Northeast Tibetan Plateau. *Earth Planet. Sci. Lett.* 288, 329–334.
- Sol, S., Meltzer, A., Burgmann, R., Hilst, R.D. v.d., King, R., Chen, Z., Koons, P.O., Lev, E., Liu, Y.P., Zeitler, P.K., Zhang, X., Zhang, J., Zurek, B., 2007. Geodynamics of the southern Tibetan Plateau from seismic anisotropy and geodesy. *Geology* 35, 563–566.
- Styron, R., Taylor, M., Okoronkwo, K., 2010. Database of active structures from the Indo-Asian collision. *EOS Trans. AGU* 91, 181–182.
- Sun, Y., Li, X., Kuleli, S., Morgan, F.D., Toksoz, M.N., Wang, Q., Zhang, P., Freymueller, J.T., Bilham, R., Larson, K.M., Lai, X., You, X., Niu, Z., Wu, J., Li, Y., Liu, J., Yang, Z., Chen, Q., 2004. Adaptive moving window method for 3D P-velocity tomography and its application in China. *Bull. Seismol. Soc. Am.* 94, 740–746.
- Sun, Y., Toksoz, M.N., Pei, S., Morgan, F.D., 2008. The layered shear-wave velocity structure of the crust and uppermost mantle in China. *Bull. Seismol. Soc. Am.* 98, 746–755.
- Tapponnier, P., Xu, Z., Roger, F., Meyer, B., Audaud, N., Wittlinger, G., Yang, J., 2001. Oblique stepwise rise and growth of the Tibet plateau. *Science* 294, 1671–1677.
- Tilmann, F., Ni, J., INDEPTH Seismic Team, 2003. Seismic imaging of the downwelling Indian lithosphere beneath central Tibet. *Science* 300, 1424–1427.
- VanDecar, J.C., Crosson, R.S., 1990. Determination of teleseismic relative phase arrival times using multi-channel cross-correlation and least squares. *Bull. Seismol. Soc. Am.* 80, 150–169.
- Velasco, A.A., Gee, V.L., Rowe, C., Grujic, D., Hollister, L.S., Hernandez, D., Miller, K.C., Tobgay, T., Fort, M., Harder, S., 2007. Using small, temporary seismic networks for investigating tectonic deformation: brittle deformation and evidence from strike-slip faulting in Bhutan. *Seismol. Res. Lett.* 78, 446–453.
- Wang, C., Gao, R., Yin, A., Wang, H., Zhang, Y., Guo, T., Li, Q., Li, Y., 2011. A mid-crustal strain-transfer model for continental deformation: a new perspective from high-resolution deep seismic-reflection profiling across NE Tibet. *Earth Planet. Sci. Lett.* 306, 279–288.
- Wang, H., Hearn, T.M., Chen, Y.J., Ni, J.F., Zhou, S., Sandvol, E.A., Yue, H., Wei, S., Tilmann, F., 2010. Pn Tomography of Eastern Tibet. 2010 Fall Meeting, AGU (abstract T43B-2211).
- Wittlinger, G., Masson, F., Poupinet, G., Tapponnier, P., Jiang, M., Herquel, G., Guilbert, J., Achauer, U., Xue, G., Shi, D., Team, L.K., 1996. Seismic tomography of northern Tibet and Kunlun: evidence for crustal blocks and mantle velocity contrasts. *Earth Planet. Sci. Lett.* 139, 263–279.
- Yang, T., Shen, Y., 2006. Frequency-dependent crustal correction for finite-frequency seismic tomography. *Bull. Seismol. Soc. Am.* 96, 2441–2448.
- Yin, A., 2000. Mode of Cenozoic east–west extension in Tibet suggesting a common origin of rifts in Asia during the Indo-Asian collision. *J. Geophys. Res.* 105, 21745–21759.
- Yin, A., Dang, Y., Zhang, M., McRivette, M.W., Burgess, W.P., Chen, X., 2007. Cenozoic tectonic evolution of Qaidam basin and its surrounding regions (part 2): wedge tectonics in southern Qaidam basin and the Eastern Kunlun Range. *Geol. Soc. Am. Spec. Pap.* 433, 369–390.
- Yin, A., Dang, Y.-Q., Zhang, M., Chen, X.-H., McRivette, M.W., 2008. Cenozoic tectonic evolution of the Qaidam basin and its surrounding regions (Part 3): structural geology, sedimentation, and regional tectonic reconstruction. *Geol. Soc. Am. Bull.* 120, 847–876.
- Han Yue, Y. John Chen, Eric Sandvol, James Ni, Thomas Hearn, Shiyong Zhou, Yongge Feng, Zengxi Ge, Andrea Trujillo, Yanbin Wang, Ge Jin, Youcai Tang, Xiaofeng Liang, Mingming Jiang, Songqiao Wei. Lithospheric and upper mantle structure of the northeastern Tibetan plateau. *J. Geophys. Res.* <http://dx.doi.org/10.1029/2011JB008545>.
- Zhao, J., Yuan, X., Liu, H., Kumar, P., Pei, S., Kind, R., Zhang, Z., Teng, J., Ding, L., Gao, X., Xu, Q., Wang, W., 2010. The boundary between the Indian and Asian tectonic plates below Tibet. *Proc. Natl. Acad. Sci.* 107, 11229–11233.
- Zhao, W., Brown, L., Wu, Z., Klemperer, S.L., Shi, D., Mechie, J., Su, H., Tilmann, F., Karplus, M.S., Makovsky, Y., 2008. Seismology across the northeastern edge of the Tibetan Plateau. *EOS Trans. AGU* 89, 487.
- Zhao, W., Kumar, P., Mechie, J., Kind, R., Meissner, R., Wu, Z., Shi, D., Su, H., Xue, G., Karplus, M., Tilmann, F., 2011. Tibetan plate overriding the Asian plate in central and northern Tibet. *Nat. Geosci.* 4, 870–873.

Supplementary materials

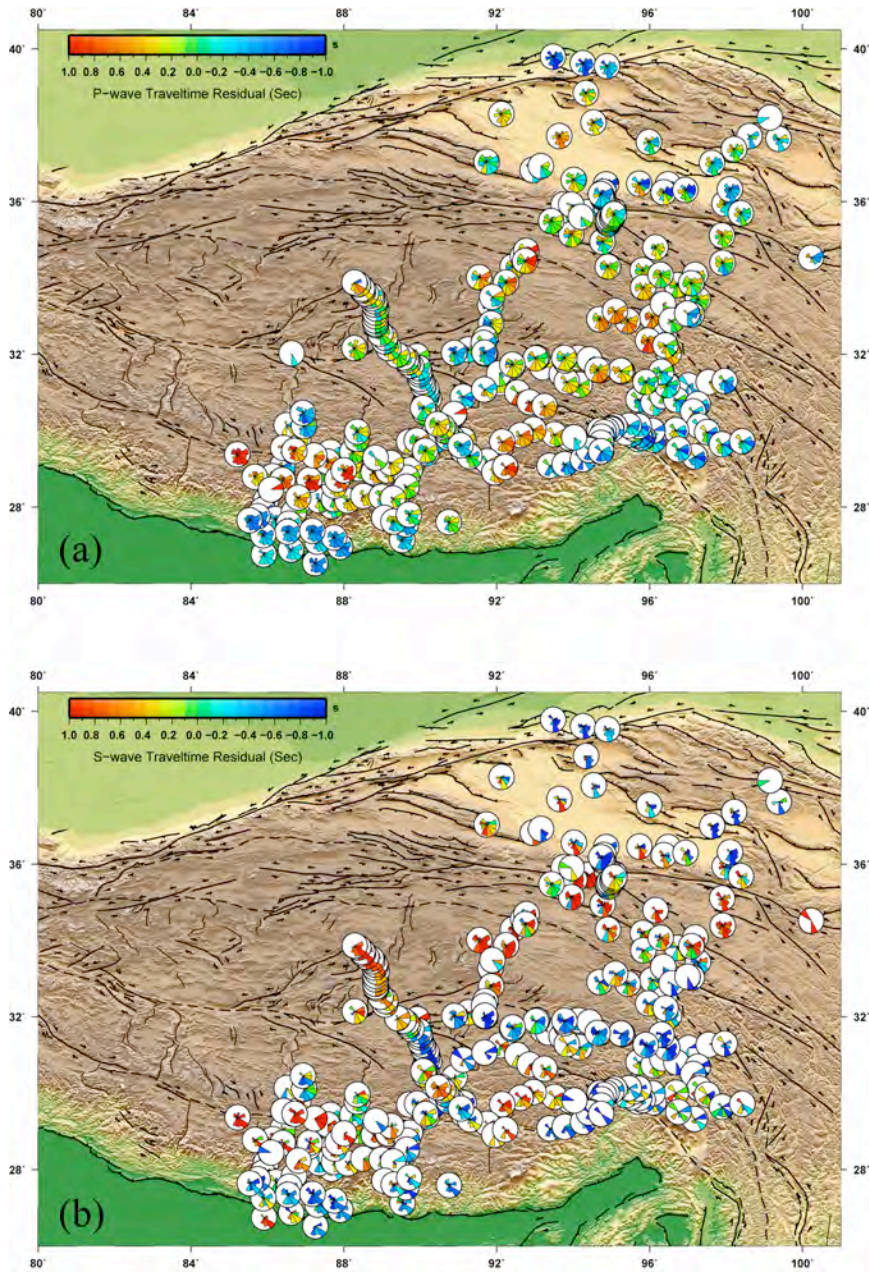


Figure S1. Sector diagrams of P- and S-wave differential travel times residuals, which is averaged in 30° azimuth space at each station. The sector length shows the normalized measurements number in the 30° azimuth range. The amplitude of measurements is shown by the different colors.

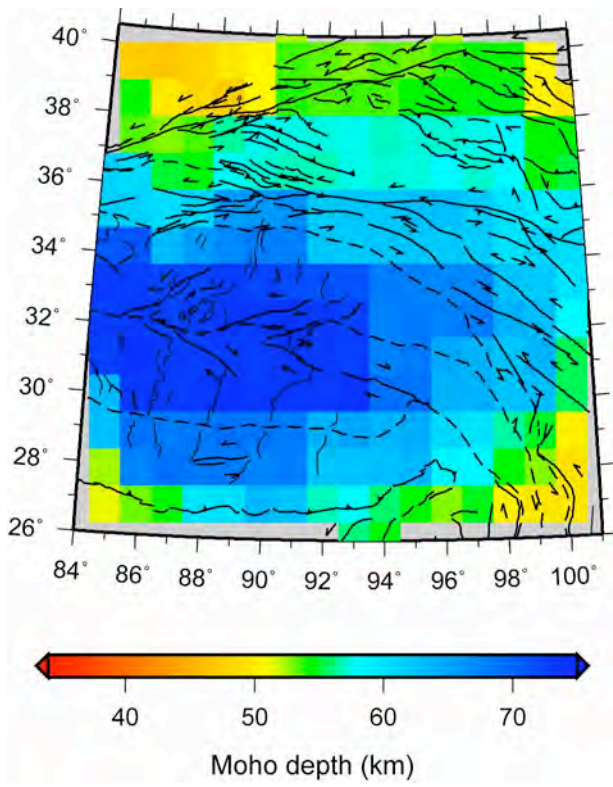


Figure S2. Moho depth map from SEAPS model.

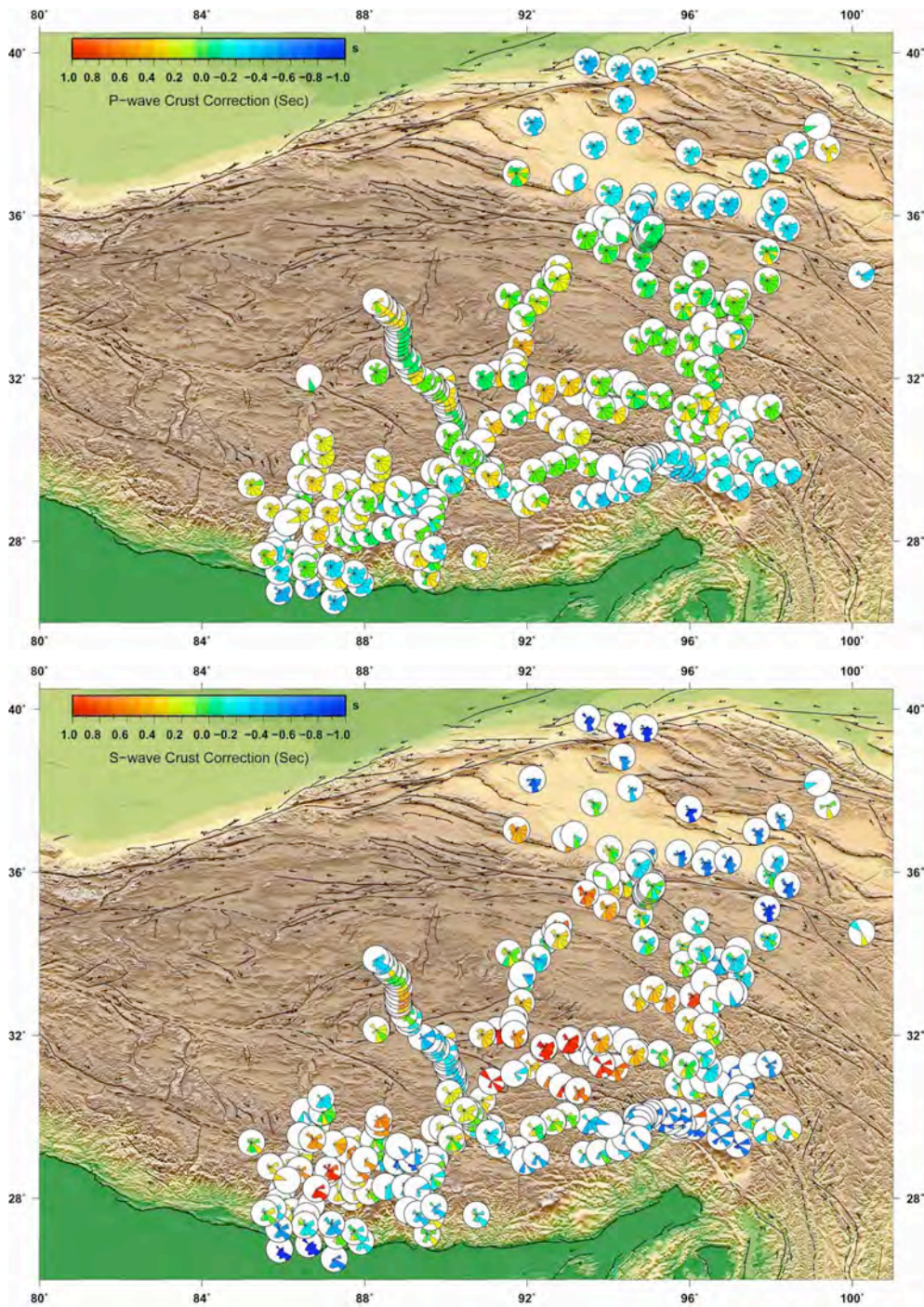


Figure S3. Crust corrections for P- and S-wave travel times calculated based on SEAPS model. The correction is calculated for each event-station pair and averaged in 30° azimuth space at each station. The sector length shows the number of normalized measurements in the 30° azimuth range. The amplitude of measurements is shown by the different colors.

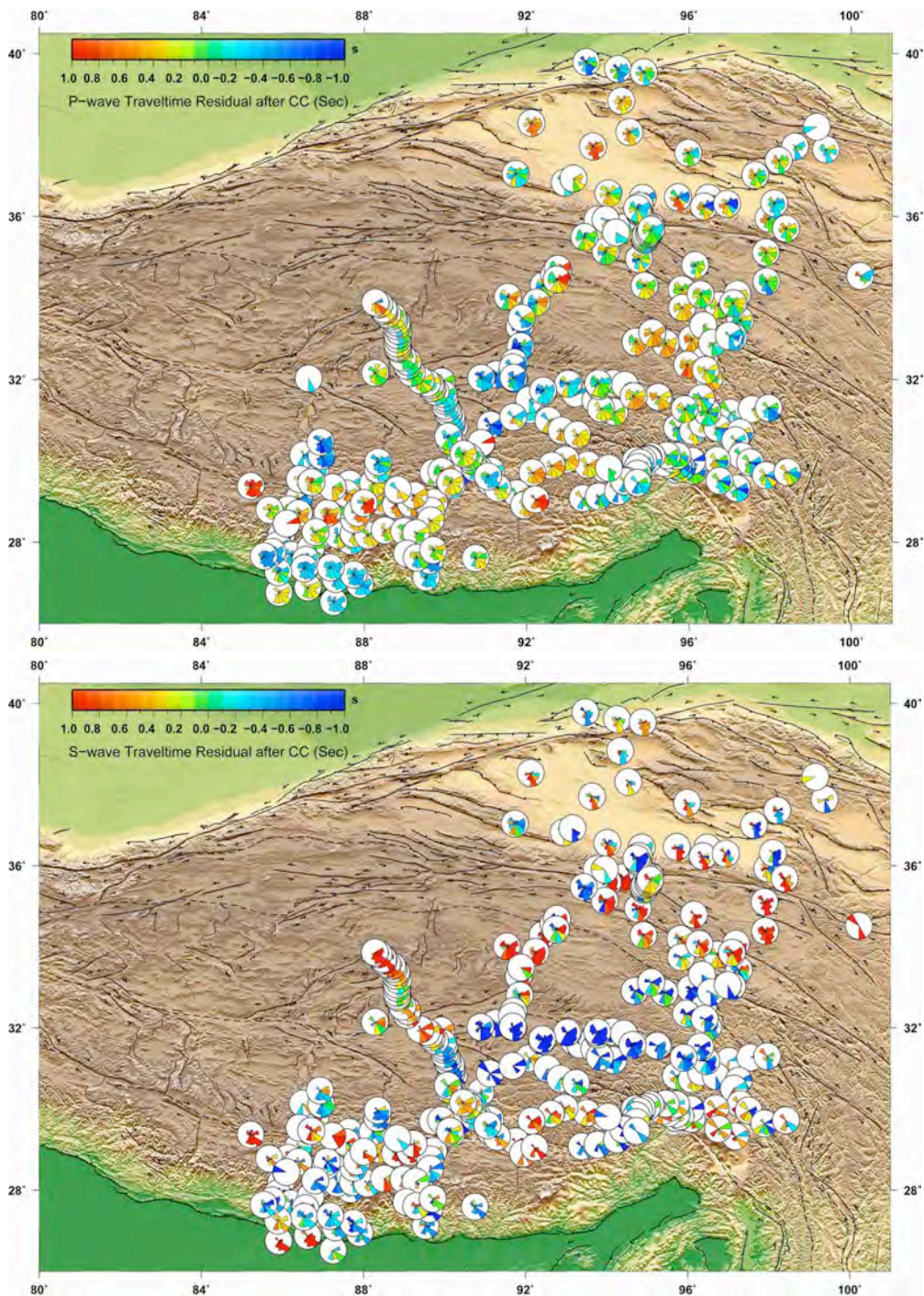


Figure S4. Sector diagrams of P- and S-wave differential travel times after crust correction (CC), which is averaged in 30° azimuth space at each station. The sector length shows the normalized measurements number in the 30° azimuth range. The amplitude of measurements is shown by the different colors.

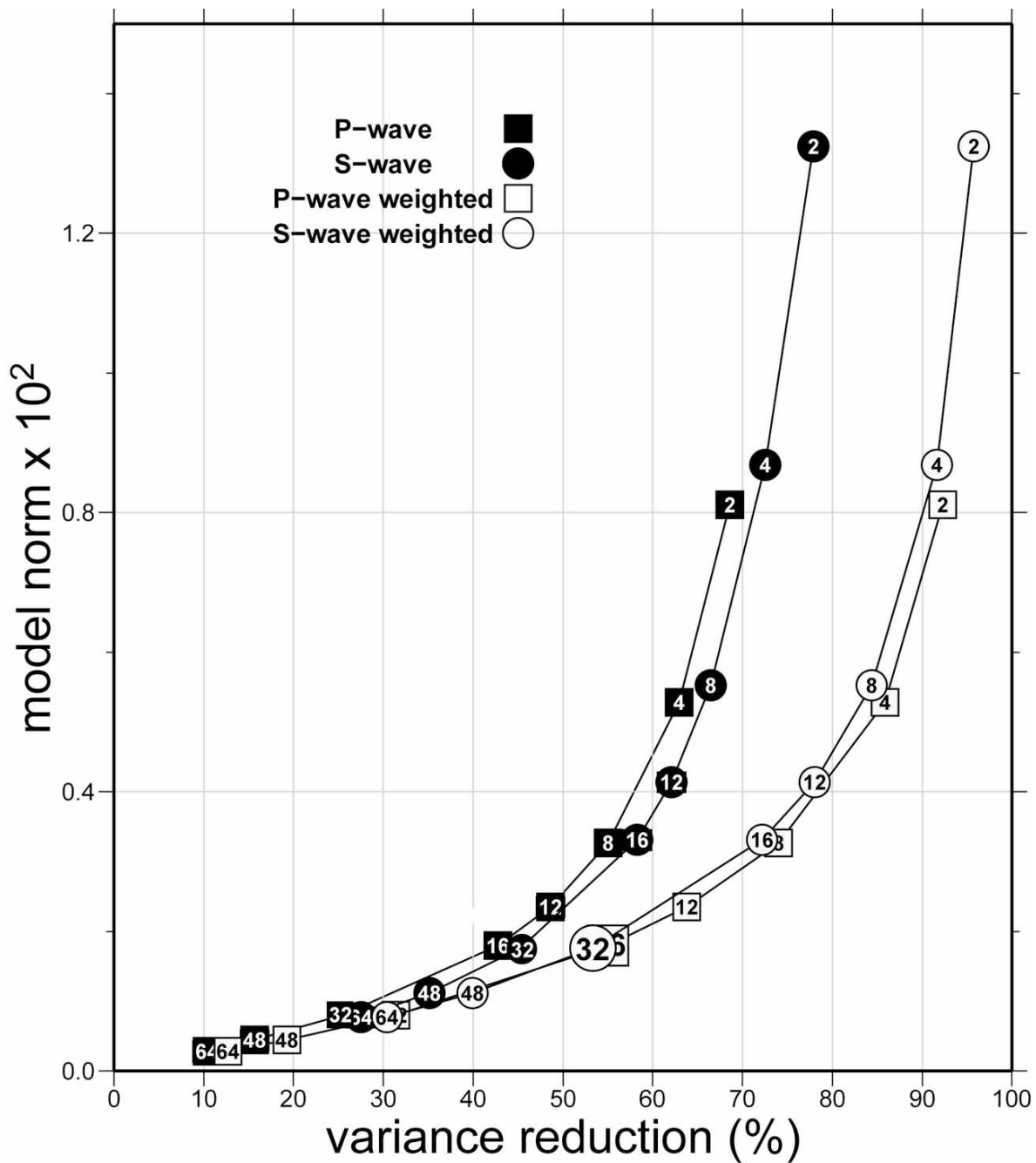


Figure S5. Tradeoff curves for both weighted and un-weighted P-, S-wave inversions. The bigger symbols show the damping parameters used in inversions. Here we define the model norm as the root-mean-square of the model perturbations, which reflects the intensity of the model parameter perturbations.

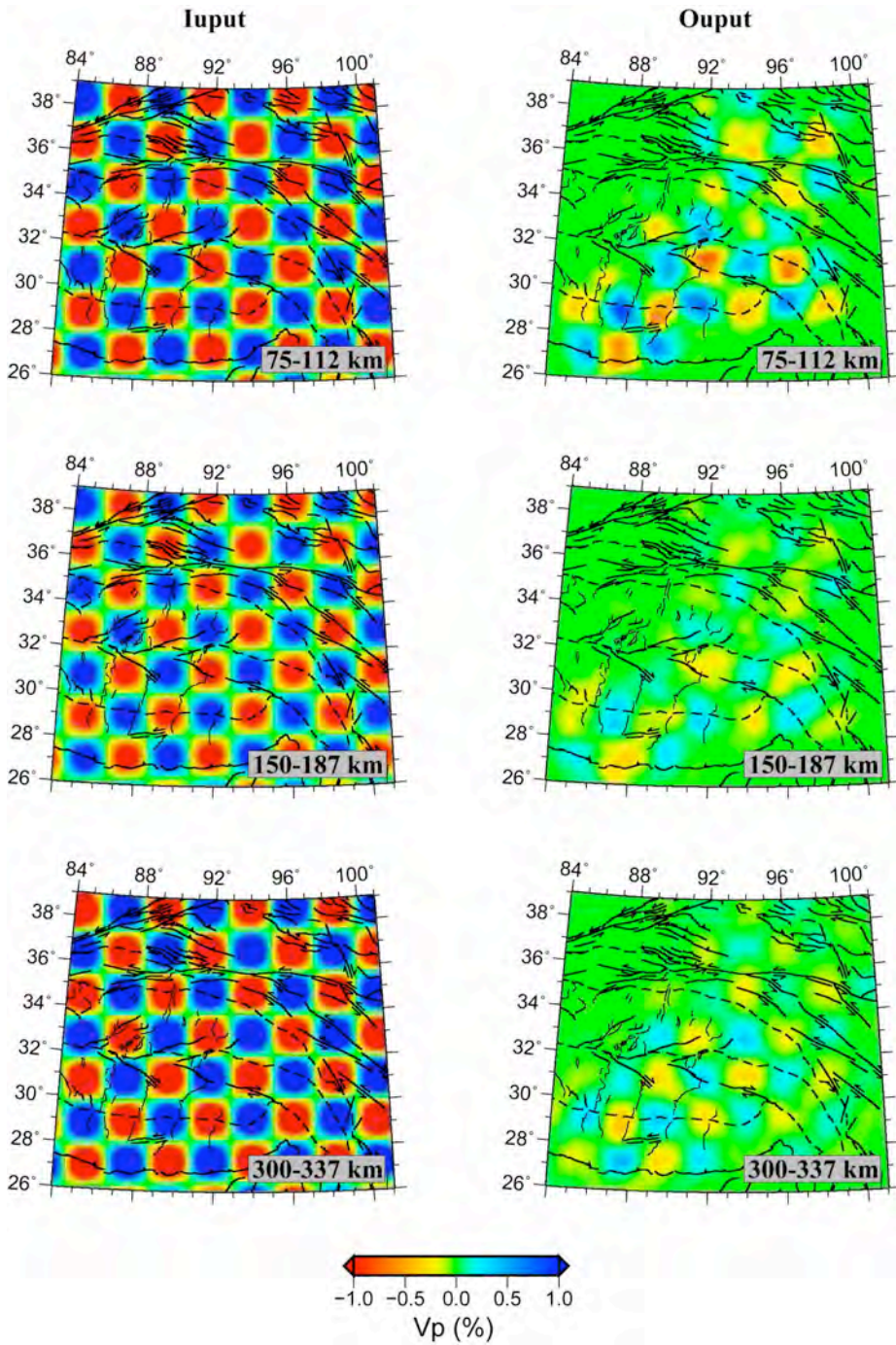


Figure S6. Horizontal (checkerboard) resolution tests for P-wave at depths of 75-112 km, 150-187 km and 300-337 km. The left column shows the input checkerboard, and the right column shows the inverted results. The inverted results are significantly damped in amplitude.

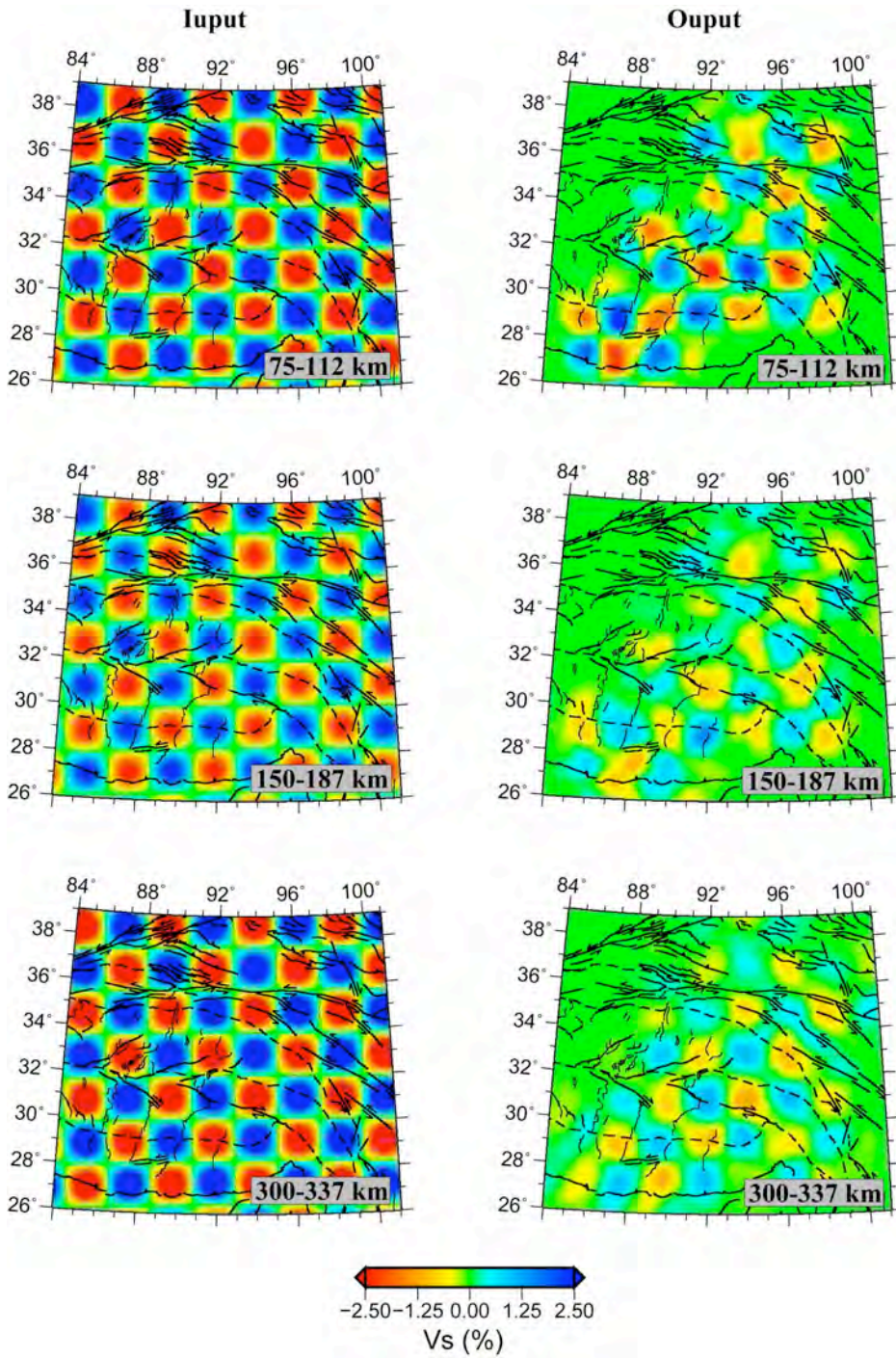


Figure S7. Horizontal (checkerboard) resolution tests for S-wave at depths of 75-112 km, 150-187 km and 300-337 km. The left column shows the input checkerboard, and the right column shows the inverted results. The inverted results are significantly damped in amplitude.

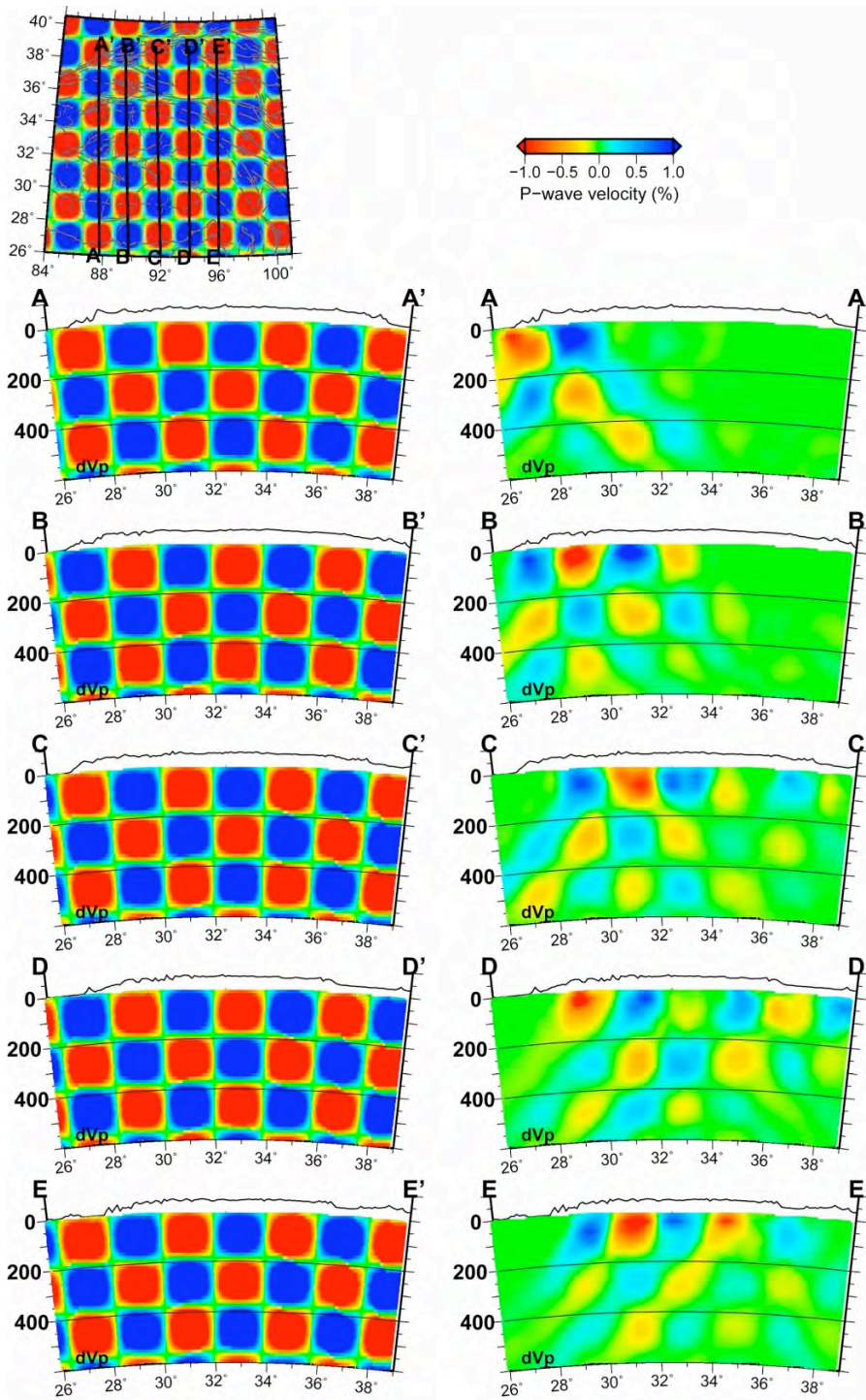


Figure S8. Vertical resolution model tests for P-wave are shown at five different cross-sections along the north-south direction. The input checkerboard has a diameter of about 150 km.

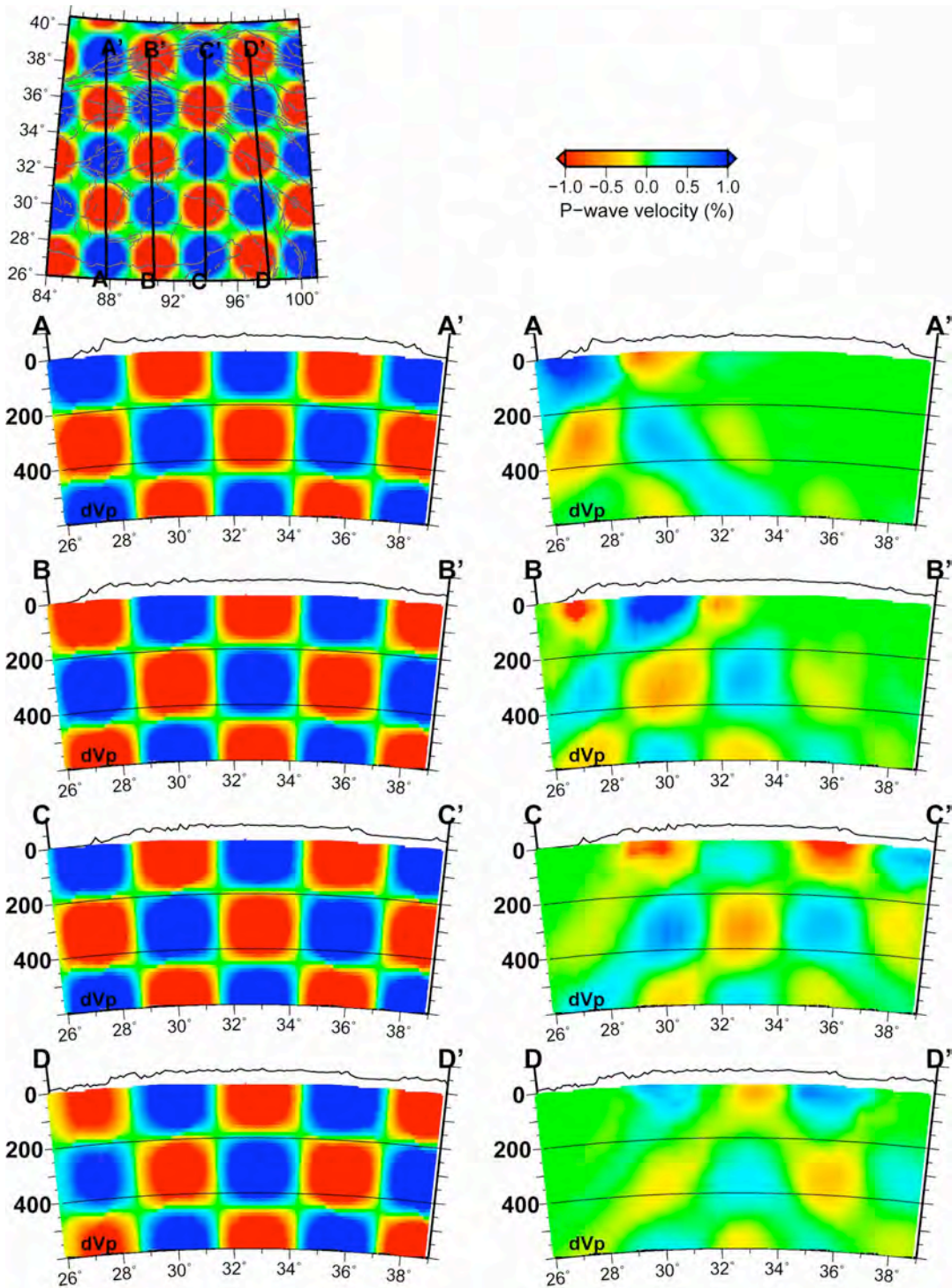


Figure S9. Vertical resolution model tests for P-wave are shown at four different cross-sections along the north-south direction. The input checkerboard has a diameter of about 225 km.

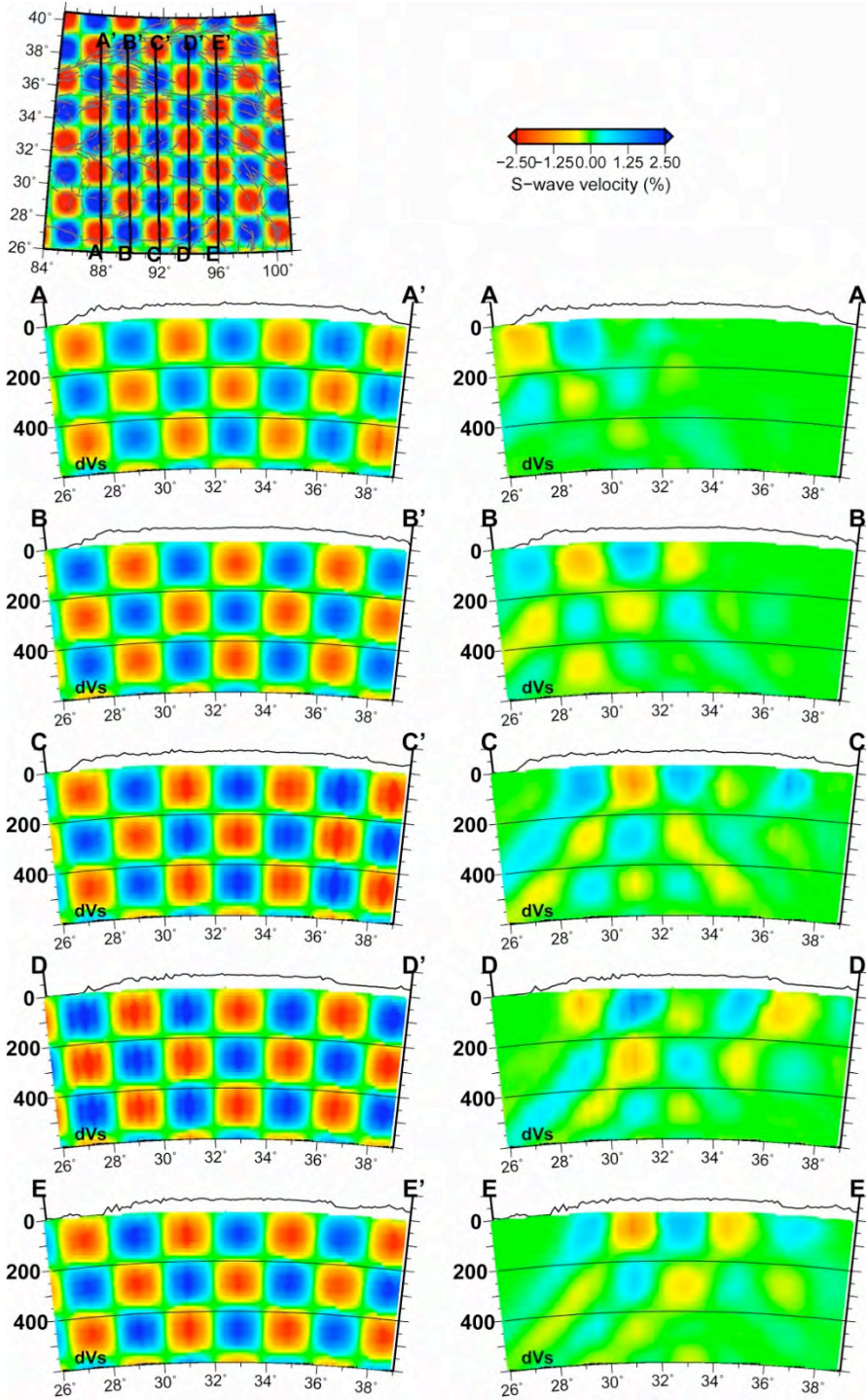


Figure S10. Vertical resolution model tests for S-wave are shown at five different cross-sections along the north-south direction. The input checkerboard has a diameter of about 150 km.

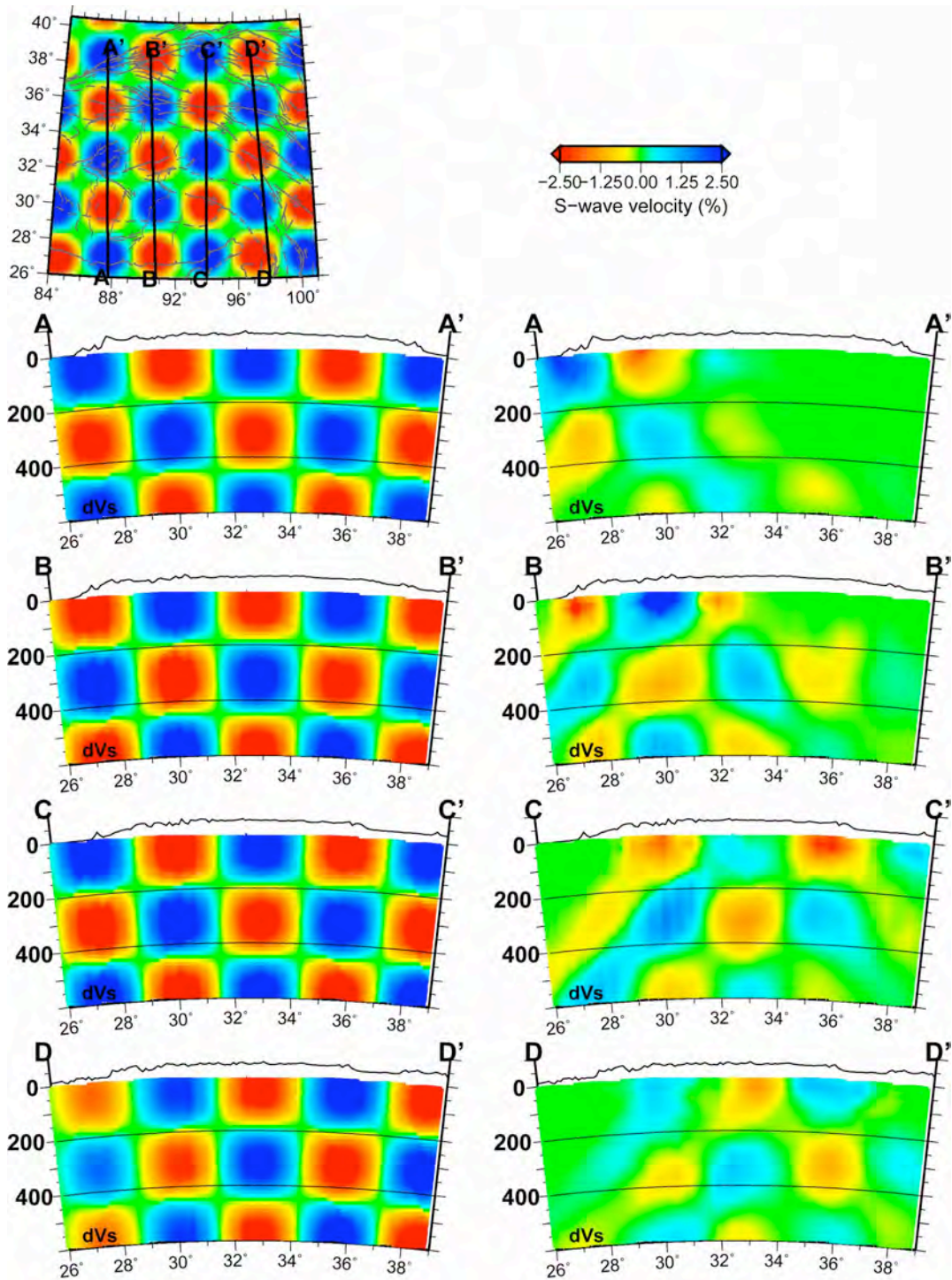


Figure S11. Vertical resolution model tests for S-wave are shown at four different cross-sections along the north-south direction. The input checkerboard has a diameter of about 225 km.

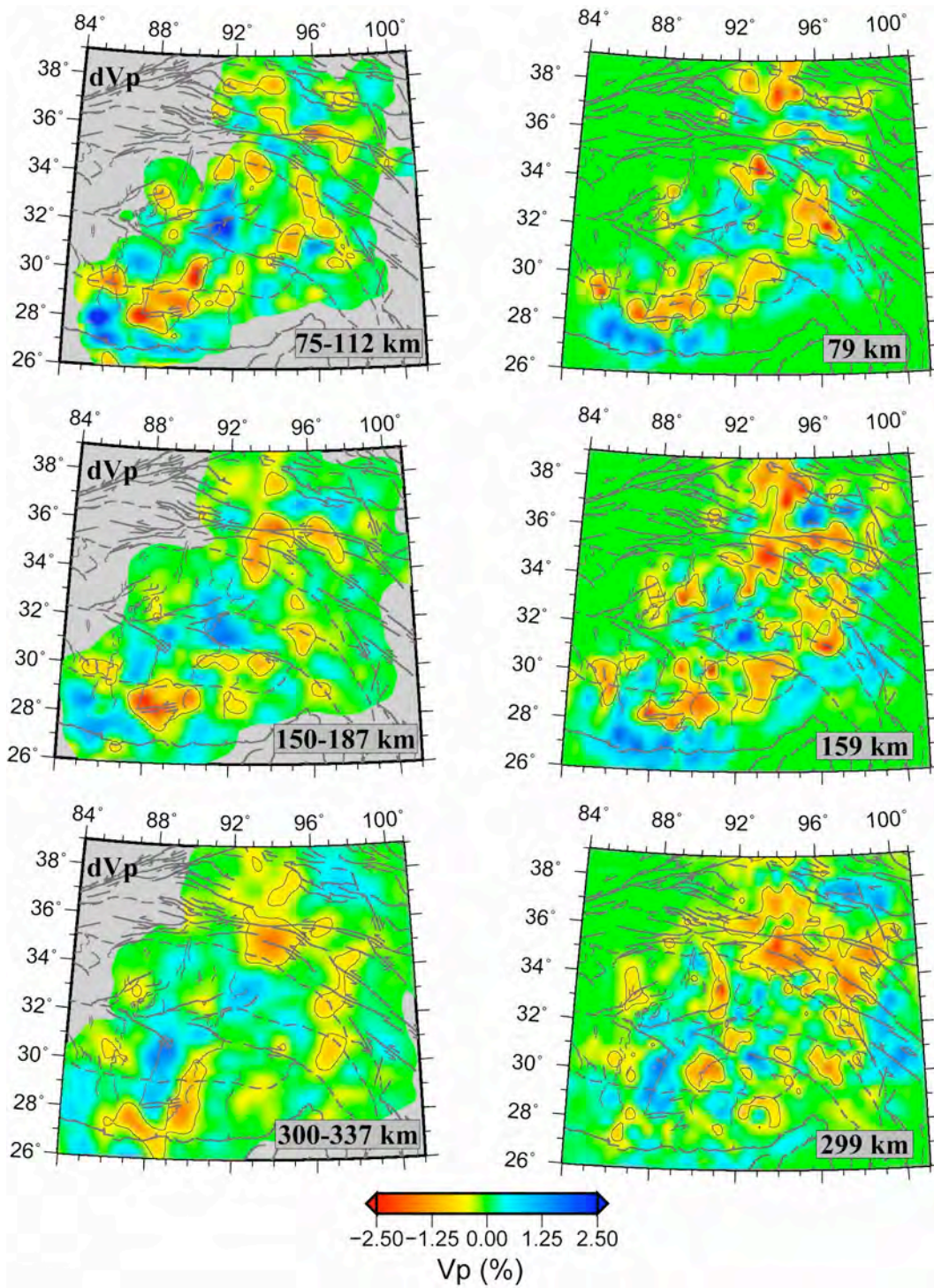


Figure S12. The comparison between the P-wave velocity perturbation from our finite-frequency images (left) and classic ray-theory images (right) at different depths.

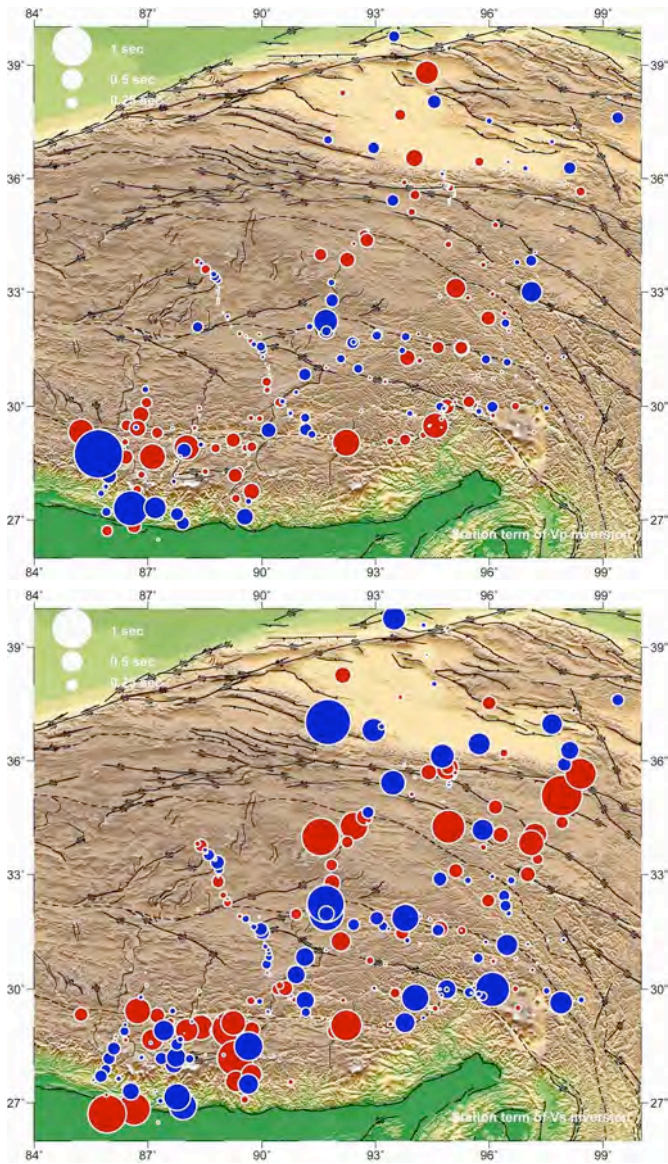


Figure S13. The station terms from both Vp and Vs inversions.